Unclassified

Project Report

NOAA-30

GOES Advanced Baseline Sounder (ABS) Point Design

M. M. Coakley

M. W. Kelly

M. E. MacDonald

D. P. Ryan-Howard

D. E. Weidler

27 November 2001

This work was sponsored by the National Oceanic and Atmospheric Administration under U.S. Air Force Contract F19628-95-C-0002.

Massachusetts Institute of Technology
Lincoln Laboratory

GOES Advanced Baseline Sounder (ABS) Point Design

Monica M. Coakley
Michael W. Kelly
Michael E. MacDonald
Danette P. Ryan-Howard
Group 97

Darryl E. Weidler
Group 75

Project Report

November 2001

Unclassified

ABSTRACT

This report documents the third in a series of point designs for the Advanced Baseline Sounder (ABS) formulated by MIT Lincoln Laboratory. This work was mandated by the evolution of ABS requirements embodied in the signed January 2001 Technical Requirements Document [1] (January 2001 TRD) issued by the National Environmental Satellite, Data, and Information Service (NESDIS), a division of the National Oceanic and Atmospheric Administration (NOAA). Earlier point designs [2][3] which had been designed to a draft set of ABS requirements [4], were not compliant with the more demanding requirements of the January 2001 TRD. The point design documented here meets all January 2001 TRD requirements, although with little to no margin in a few key areas (coverage rate, NEdN, and data rate). Along with the two previous point designs, it also demonstrates the impact of increasing technical requirements on an advanced sounding instrument. As of this writing, another version of the TRD may be written. Thus the TRD mentioned here is the January 2001 TRD.

EXECUTIVE SUMMARY

This report culminates a series of studies carried out at the request of the National Oceanic and Atmospheric Administration (NOAA) to formulate a point design for an advanced sounding instrument for the Geostationary Operational Environmental Satellite (GOES) platform.

A substantial volume of material that forms the basis of this point design may be found in an earlier study [2], which focused on the architectural trades for an advanced sounding instrument. The differences between the point design documented here and that of the earlier study arise from differences in the outcomes of the individual trades when they were re-evaluated in light of the NESDIS January 2001 TRD requirements, which are summarized in Section 1 of this document. In particular, this point design incorporates active refrigeration of the focal planes with a cryocooler, and the optical field and detector focal-plane array (FPA) format have been broadened to provide faster coverage. The Fourier-transform Michelson spectrometer (FTS) architecture has been retained because it was sufficient to meet the January 2001 TRD requirements. This does not prejudge the ability of a dispersive instrument architecture to meet these requirements as well.

The recommendation of this study is that a high-resolution atmospheric sounder based on an FTS architecture will meet the January 2001 TRD requirement set. Although we expect that some optimization of the point design documented here is possible, the design meets January 2001 TRD requirements in many respects (coverage, NEdN, and data rate to name a few) with zero margin. Clearly, at this early conceptual stage, there are risk implications, and efforts to mitigate this risk are expected to be ongoing.

As a further elaboration, the NEdN is "met" in the sense that *median* pixel NEdN (see Figure 2-19 in Section 2.5.1 and Figure 2-32 in Section 2.8.1) is compliant with the January 2001 TRD threshold over *most* of the relevant spectral regions. Further proof that the point design is compliant with the January 2001 TRD NEdN requirement (which is derived from the NWS sounding accuracy requirement) is provided by Figure 2-34 and Figure 2-35 in Section 2.8.2. This figure illustrates that the *intent* of the January 2001 TRD requirement is met - namely, the accuracy of retrieved soundings is expected to be within the ±1 K RMS threshold of the NWS ORD (again, over *most* of the relevant vertical layers). There is no easy way to specify observational or radiometric and noise performance rigorously and unambiguously. The NWS ORD and NESDIS January 2001 TRD are meant to give contractors design flexibility in meeting the needs of the end users. From a cost-benefit viewpoint, this is certainly the proper approach. Nevertheless, much of the motivation of this work was to identify issues such as those noted in this paragraph early in the ABS procurement process, and the requirements definition process is ongoing.

A concise summary of the point design is presented in Figure 1 and Table 1. Details of the point design are contained in Section 2 of this document.

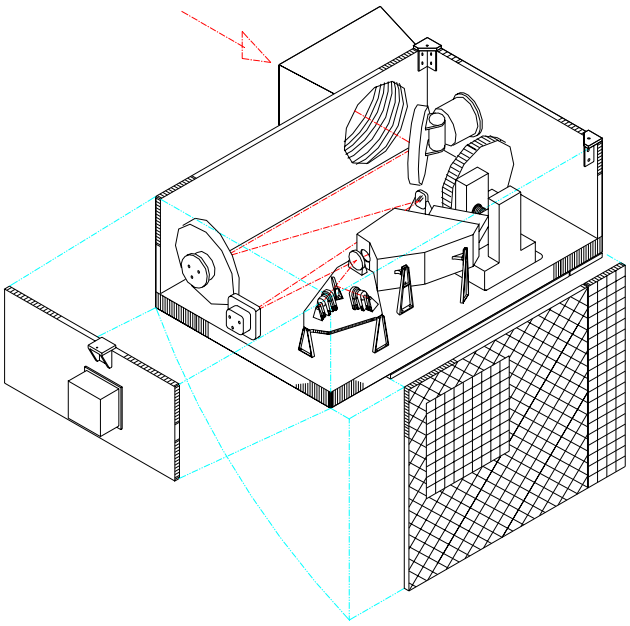

Figure 1. An exploded view of the ABS point design (electronics box not shown).

Table 1. ABS Instrument Summary

Feature	Description
Optical aperture	30.48 cm (12 in.)
Scan method	2-axis step & dwell, step size reduced as required to compensate for image rotation. 6.05 mrad (220 km SSP) nominal steps E-W 13.2 mrad (480 km SSP) nominal steps N-S
Dwell time	3.0 s
Coverage rate	6.4 x 10^7 km^2 in 60 min, not including any overlap or edge effects See Figure 1-2
Spatial resolution	278 μrad square (10 km x 10 km SSP)
Spectral resolution	2.5 cm^{-1}, 2150 - 2720 cm^{-1} (shortwave band) 1.25 cm^{-1}, 1210 - 1740 cm^{-1} (midwave band) 0.625 cm^{-1}, 650 - 1200 cm^{-1} (longwave band)
Input telescope	Three-mirror, re-imaging, afocal telescope
Interferometer	Michelson interferometer, 3.3 cm beam dia., ZnSe beamsplitter, flexure-bearing moving mirror in one arm, commandable mirror in second arm.

Feature	Description
Interferometer mirror sweep	$\pm$ 0.4 cm, RMS velocity fluctuation < $\pm$0.1%
Aft optics	Catadioptric, field-imaging, *f*/0.85 optics
Visible channels (full-albedo and low-light, unless otherwise noted)	Silicon 1024x1024 CCDs (220 x 480 subframe used), 12 μm pixels, 28 μrad pixel FOV (1 km SSP), 298 K stabilized temperature Full albedo channel: 2.4% optical throughput, SNR=548 for 3 ms integration, 1 km FOV Low-light channel: 43% optical throughput, SNR=115 for 3 s integration, 1 km FOV (full moon) SNR=29 for 3 s integration, 1 km FOV (quarter moon) SNR=13 for 3 s integration, 1 km FOV (nautical twilight)
Star sensing	8 Tracking operations per hour, annulus between 17.3^o (Earth limb) and 25^o (lookup table / database assumed) SNR=158 for 1 s integration, 4th magnitude star SNR=34 for 1 s integration, 7th magnitude star
IR Detector focal planes (all bands, unless otherwise noted)	Photovoltaic HgCdTe, 22 x 48 arrays, 58 μm wide pixels on 72 μm pitch. 278 μrad sq. pixel FOV (10 km SSP), 145 μs integration time (6.9 kHz frame rate), LW band. λ_{cutoff} = 4.7 μm, SW FPA operating at 65 K, λ_{cutoff} = 8.5 μm, MW FPA operating at 65 K, λ_{cutoff} = 15.1 μm, LW FPA operating at 65 K.
IR focal plane readouts (all bands, unless otherwise noted) IR focal plane readouts (cont'd)	Custom Readout, 3.8 x 10^8 e^- LW charge storage, 94 μV LW & MW ROIC noise. CTIA SW preamp, BDI MW and LW preamps. One SW output tap, 7.2 MHz, 8 MW output taps, 450 KHz each, 16 LW output taps, 450 KHz each.
Data quantization	12-bit vis., 12-bit SWIR, 16-bit MWIR & LWIR
Cryocooler configuration	Fully redundant pulse-tube coolers, no heat switching, redundant electronics. 60 K cold tip temperature, 250 K reject temp. 2.5 W load @ 60 K, 20 W/W specific power.
Passive cooler configuration	α = 0.17 EOL, ε = 0.78 EOL, rear-surface silvered glass. 200 K radiator: 0.22 m^2, 10.2 W 250 K radiator: 0.41 m^2, 70 W 300 K radiator: 0.11 m^2, 40 W
Calibration blackbody and calibration intervals	290 K full-aperture blackbody, 15 min. interval
Predicted channel NEdN viewing 289 K blackbody (FPA median values at band centers)	SWIR: 0.009 mW/(m^2 cm^{-1} sr), MWIR: 0.05 mW/(m^2 cm^{-1} sr), LWIR: 0.13 mW/(m^2 cm^{-1} sr).
Predicted retrieval accuracy (for information only)	surface-300 mb: $\leq\pm$1.0 K, $\leq\pm$10% RH, 300-100 mb: $\leq\pm$1.0 K, $\leq\pm$20% RH, above 100 mb: $\leq\pm$1.0 K.
Instrument power consumption	~ 235 W
Instrument mass	~ 185 Kg

Feature	Description
Instrument dimensions	See Figure 2
Instrument data rate	10 Mbps

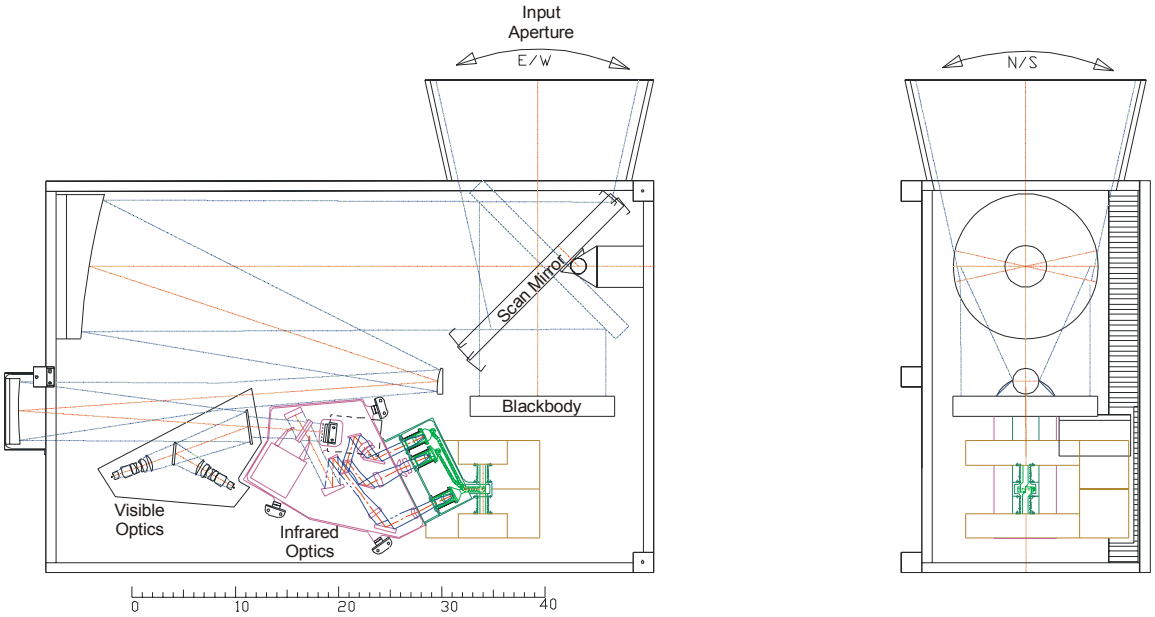

Figure 2. The ABS sensor volume.

The operation of the ABS point design is now briefly summarized, referring to Figure 1: Radiance from the Earth scene is collected by a 30 cm diameter aperture which is baffled to reduce the influx of sunlight into the instrument. The scene radiance is directed to the input telescope by a scan mirror with two angular degrees of freedom. The mirror steps the 220 km (E-W) by 480 km (N-S) instrument field-of-view over the Earth scene, and slews to allow the instrument to view either the internal blackbody or cold space for radiometric calibration. The telescope collects the scene radiance and passes it to a dichroic, which passes the infrared portion to the Michelson interferometer, and reflects the visible portion. The visible radiance is divided between two silicon charge-coupled detector (CCD) arrays, with the majority of the radiance going to a low-light imaging CCD, and the remainder passed to the daylight imaging CCD. Together, these detector arrays serve to provide visible imagery for cloud-cover detection, and star-sensing capability for image navigation and registration. The scan mirror, input telescope, and visible optics are mounted to an ambient-temperature optical bench.

The Michelson interferometer divides the IR radiance equally between two arms terminated in mirrors. The optical path difference (OPD) between these arms is modulated by displacing one mirror to produce a time-varying interference pattern when the reflected beams are recombined at the beamsplitter. The second mirror uses a commandable actuator for post-launch alignment of the interferometer. A near-IR laser is injected alongside the IR beam in the interferometer such that it provides knowledge of the position and velocity of the moving mirror, along with the mirror tilt error. This metrology beam provides triggering knowledge for the detector array sampling electronics. The output of the Michelson interferometer is relayed through dichroics and the aft optics to three photovoltaic detector focal planes optimized for shortwave-infrared (SWIR), midwave-infrared (MWIR) and longwave-infrared (LWIR) regions. The aft optics configuration images the Earth scene onto the detector arrays. The Michelson interferometer beamsplitter/compensator and the aft optics are mounted to an optical bench kept thermally isolated from the ambient-temperature optical bench. This bench is cooled to 200 K by a passive radiative cooler located on the North- (or South-) facing side of the sensor exterior. Kinematic mounts align this bench to the ambient-temperature optics, which maintain warm-to-cold alignment.

Each focal plane is implemented as a 22 x 48 pixel array of photovoltaic (PV) $Hg_{1-x}Cd_xTe$ that is Indium bump-bonded to a silicon readout IC that provides integration, preamplification, and readout-multiplexing functionality through serial output channels. The detectors are located in a vacuum enclosure and are connected through thermal straps to a redundant pair of pulse-tube cryocoolers, which allow the detectors to be controlled at 65 K. Vibrational decoupling between the cryocoolers and detectors is provided. The Cryocoolers are sunk to a 250 K passive radiative cooler which is coplanar with the 200 K radiator, and which surrounds it to reduce parasitic heat input from the sensor.

The detected signal is in the form of an interferogram, which contains the spectral information for each pixel encoded in the time domain. This signal is integrated and sampled at OPD intervals determined by the metrology system. It is then amplified, digitized, and routed to digital signal processing electronics that impose a decimating finite impulse-response (FIR) digital filter on the over-sampled data. These signal-processing functions are implemented in redundant electronics modules external to the ABS sensor. The resulting data stream is combined with visible data and sensor telemetry and passed to the spacecraft. Control circuits for the scan mirror, moving mirror, instrument and instrument temperature are housed external to the ABS sensor in a redundant electronics and power supply module. Redundant cryocooler control electronics are external to the sensor as well.

Apart from its mass, volume, power, and data stream, and any necessary image motion compensation measures, the instrument operates independently of the satellite bus. For the purposes of motion compensation, most uncompensated momentum is constrained to the N-S axis, as is presently the case for GOES instruments (implying E-W scanning preference). Although the use of a "yaw flip" to eliminate solar illumination of the passive radiators is assumed in their sizing, only the 200 K radiator would otherwise require a sunshade. The 300 K radiator has adequate room for growth to handle solar illumination. The 250 K radiator would operate near ambient temperature under illumination, with a ~30

W increase in sensor power consumption due to reduced cryocooler efficiency. The presence of a 4x1 m solar array in the radiator FOV is assumed.

ACKNOWLEDGMENTS

The authors gratefully acknowledge Dan Mooney, Greg Berthiaume, and Ed Bicknell of MIT/LL for consultation on technical issues. We also appreciate guidance on science requirements from Paul Menzel and Tim Schmit of the National Environmental Satellite, Data, and Information Service (NESDIS). We are grateful to Trish Hardy, Jacqueline Pettingell and Cynthia Wallace for their assistance in preparing the manuscript and to Jane Luu for her editorial comments.

TABLE OF CONTENTS

TABLE OF CONTENTS
(Continued)

Page

LIST OF ILLUSTRATIONS

LIST OF ILLUSTRATIONS
(Continued)

Figure No. **Page**

LIST OF TABLES

1. ABS REQUIREMENTS

1.1 Requirements Overview

The work documented in this report was motivated by the issuance of a formal set of engineering requirements for the Advanced Baseline Sounder. The process by which the requirements are defined is ongoing as this report is being written, and it is illustrated schematically below in Figure 1-1. Throughout this process, the responsibility for defining system requirements flows gradually from end users such as the National Weather Service (NWS) to the procuring authority, which is the National Aeronautics and Space Administration (NASA). There is a similar evolution in the nature of the requirements from generalized observations of the Earth surface and atmosphere to specific instrument engineering details.

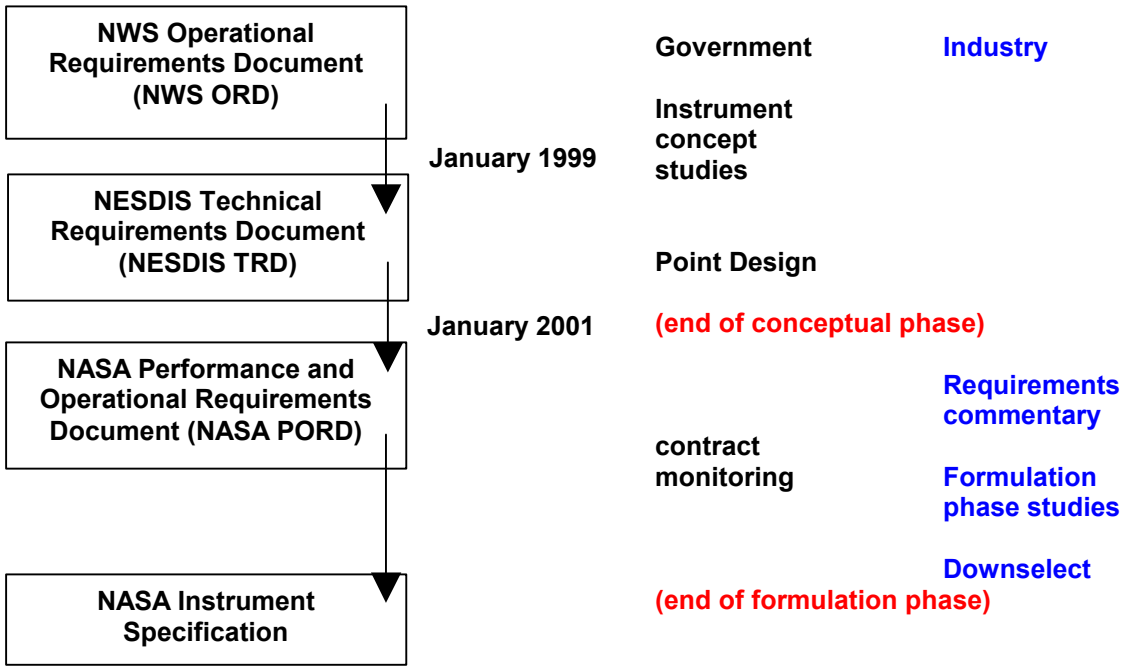

Figure 1-1. The ABS requirements definition process.

The first point design [2] formulated by MIT/LL occurred early in this process while the top level NWS requirements were still in draft form [4]. Although the second MIT/LL point design [3] was formulated

after the issuance of the final NWS requirements [5], which differed substantially from the draft document, this point design was intended only to be a minor modification to improve spatial performance while the NWS requirements were evaluated by NESDIS.

This review of ABS requirements by NESDIS culminated in their issuance of a Technical Requirements Document [1] (TRD), which sets forth the formal system engineering requirements implied by the NWS observational requirements. The substantial upgrade in requirements for observational capability between the draft and final NWS document is reflected in a January 2001 TRD which was no longer satisfied by either of the two MIT/LL point designs, particularly in coverage rate and noise-equivalent differential radiance (NEdN). As a means of validating these key January 2001 TRD requirements, the point design documented in this report was formulated.

The final evolution of ABS requirements is embodied in a NASA-issued Performance and Operational Requirements Document (PORD), which governs a competitive procurement of instrument designs from potential ABS contractors. At the time of this writing, the PORD is being defined and the TRD may be modified. In the wake of this, the final requirements governing the ABS flight instrument(s) procurement will be formulated.

1.2 Requirements from the NESDIS January 2001 TRD

The requirement set relevant to this work is the NESDIS January 2001 TRD. This document extracted and interpreted atmospheric sounding requirements from the NWS ORD, and incorporated additional requirements such as spectral coverage, radiometric sensitivity and mission lifetime. A summary of the observational requirements from the NWS ORD is included as Table 1-1. Because these observational requirements are not bench-testable at the instrument level, they did not form part of the NESDIS January 2001 TRD, and are included here for information only.

Table 1-1. NWS ORD Sounding Performance Summary: Accuracies and vertical resolution in clear air (for information only)

Altitude Range	Observational Accuracy		Observational Accuracy		Vertical Resolution	
	Temperature THRESHOLD	Temperature GOAL	Humidity THRESHOLD	Humidity GOAL	THRESHOLD	GOAL
Surface-500 hPa	±1.0 K	±0.5 K	±10%	±5%	0.3 - 0.5 km layers	< 0.3 - 0.5 km layers
500-hPa-300 hPa	±1.0 K	±0.5 K	±10%	±5%	1 - 2 km layers	< 1 - 2 km layers
300 hPa-100 hPa	±1.0 K	±0.5 K	±20%	±10%	1 - 2 km layers	< 1 - 2 km layers
100 hPa and above	±1.0 K	±0.5 K	N/A	N/A	2 - 3 km layers	< 2 - 3 km layers

The system requirements implied by these observational needs were set forth in the NESDIS January 2001 TRD. These requirements formed the specifications for this point design, and the primary input into the NASA PORD, which governs design work by industry during the formulation phase (Phase B). The January 2001 TRD requirements are summarized in Table 1-2.

Table 1-2. The NESDIS January 2001 TRD requirement set for ABS (partial list)

Requirement		Threshold
Spatial resolution	Visible	1 km IFOV to enable accurate cloud-cover detection
	IR	10 km (280 μrad) square
Ensquared energy (all bands)		At least 90% of the response detected in a sample must originate from a 10x10 km ground sample corresponding to this FOV.
Spatial coverage rate	The region within 62° local zenith angle (except only half the overlap region between two satellites). See Figure 1-2	Each hour, including any necessary allowance for IR calibration and star sensing. Operational scenarios may deviate from scanning the area every hour, but this coverage rate is needed to provide both CONUS and a minimum adequate level of ocean coverage.
	Regional and mesoscale, when required	Must be supported and selectable
Visible imaging star sensing		4 stars per half hour
Operation during eclipse		Yes
Timeliness of radiance data		3 minutes
Simultaneity		Within 10 sec. for all bands at any FOV (limits cloud encroachment into FOV to 10%)
Data format		Native (no resampling to fixed grid)
Navigation (Vis. and IR)		≤ 2.5 km (≤ 70 μrad) at SSP
Registration within frame (Vis. and IR)		≤ 2.0 km (≤ 56 μrad) at SSP
Registration image-to-image	Visible	≤ 2.5 km (≤ 70 μrad) in 30 min
	IR	≤ 2.5 km (≤ 70 μrad) in 30 min
Band-to-band coregistration	Visible-IR	≤ 1.0 km (≤ 28 μrad) at SSP
	IR-IR	≤ 1.0 km (≤ 28 μrad) at SSP (≤ 10% of FOV)
IR spectral bands and spectral resolution	Shortwave IR	2150-2720 cm^{-1}; 2.5 cm^{-1} (228 spectral bins)
	Midwave IR	1210-1740 cm^{-1}; 1.25 cm^{-1} (424 spectral bins)
	Longwave IR	650-1200 cm^{-1}; 0.625 cm^{-1} (880 spectral bins)
IR band Radiometric sensitivity (maximum NEdN) when viewing 289 K blackbody test target at nominal spectral resolution	650 - 670 cm^{-1} (LWIR)	1.0 mW/(m^2 sr cm^{-1})
	670 - 685 cm^{-1} (LWIR)	0.7 mW/(m^2 sr cm^{-1})
	685 - 700 cm^{-1} (LWIR)	0.5 mW/(m^2 sr cm^{-1})
	700 - 1150 cm^{-1} (LWIR)	0.15 mW/(m^2 sr cm^{-1})
	1150-1200 cm^{-1} (LWIR)	0.3 mW/(m^2 sr cm^{-1})
	1210-1740 cm^{-1} (MWIR)	0.06 mW/(m^2 sr cm^{-1})
	2150-2720 cm^{-1} (SWIR)	0.008 mW/(m^2 sr cm^{-1})
Visible band sensitivity		300:1 SNR at full albedo, 0.52 to 0.70 μm

Requirement		Threshold
IR band calibration		Full-aperture, independent of scan position, Absolute brightness-temperature accuracy ± 1.0 K, relative brightness-temperature accuracy ± 0.1 K (1-sigma) line-line, detector-detector, channel-channel, calibration-calibration
Maximum data rate		10 Mbps
Lifetime	Ground storage	2 years
	On-orbit storage	3 years
	Mean mission life	8.4 years
	ABS design life	10 years

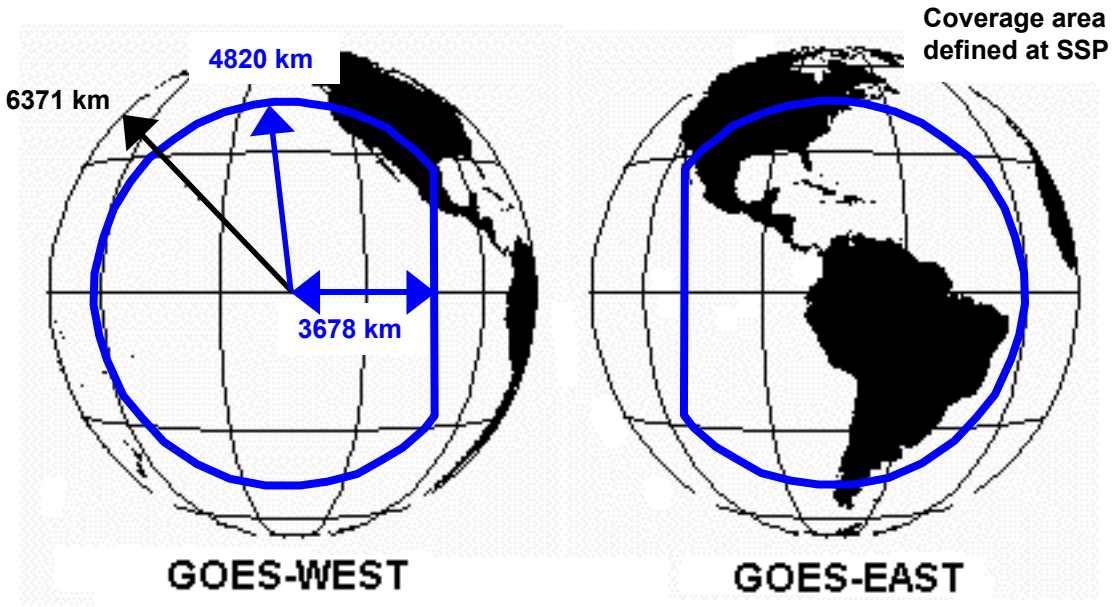

Figure 1-2. The coverage area implied by the 62° local zenith angle requirement is illustrated, along with the effect of removing the overlap zone between GOES-East and GOES-West.

1.3 "Top Priority" Requirements

In addition to the above requirements, two ABS parameters were specified as "top priorities" in the NESDIS January 2001 TRD. Each of these had earlier been flagged in the NWS ORD. These are:

1. The spatial coverage rate cited in Table 1-2, and in Figure 1-2.

2. The need for the sounder to operate continuously during periods in which it is eclipsed (shadowed from sunlight by the Earth). Moreover, so-called "keep-out zones" near the sun when it approaches the Earth limb must be reduced such that areas further than 10^{o} from the sun experience no loss of data quality, while areas between 3^{o} and 10^{o} from the sun have NEdN performance no worse than twice the threshold values of Table 1-2.

1.4 Spacecraft Interface Design Goals

Although no specific spacecraft accommodation issues were defined by the NESDIS January 2001 TRD (except the data rate, which is limited by the GOES downlink frequency allocation), the following goals were defined:

1. Mass and volume no greater than the existing sounder to maintain compatibility with the GOES N-Q bus design, electronics and cabling, and size and location of the instrument slot.

2. Power consumption no greater than the GOES N-Q sounder under normal operating conditions.

3. Passive radiative cooling of the instrument is preferred (though not mandated).

2. ABS POINT DESIGN

2.1 Overview

The point design presented in this section evolved from two earlier Michelson interferometers used as Fourier Transform Spectrometers (FTS) point designs [2][3] which provided a framework for arriving at an instrument design compliant with the January 2001 TRD requirements. Reference 2, in particular, presented numerous architectural trades that were evaluated in formulating the first ABS point design. Several, but not all, of these trades were re-evaluated in this work.

In particular, the decision was made not to re-open the trade between an FTS and a dispersive instrument architecture. This was done primarily because it was recognized early on that an FTS could be configured as described here to meet the January 2001 TRD requirements. A secondary reason was that three MIT/LL point designs have been generated, as requirements are made more stringent, which serve to demonstrate the evolution of an FTS sounder. That this design meets the January 2001 TRD does not rule out a dispersive instrument meeting the January 2001 TRD as well, within acceptable budgets for mass, power, volume, cost, and risk.

2.2 ABS Coverage and Scan Strategy

The coverage area shown in Figure 1-2 was used in conjunction with a 1-hour refresh time to define the true intent of the January 2001 TRD coverage requirement, which is a coverage *rate*. ABS is required to cover the area encompassed by 62 degrees local zenith angle in hour. The coverage area corresponding to the ABS January 2001 TRD threshold is a 4820 km radius disk at SSP with a sector removed at a distance 3678 km from SSP. Including edge effects at the end of the rows, the total area covered is equivalent to a disk with a radius of 4919.5 km. Each image of the array, or projected footprint, will experience image rotation due to the motion of the mirror gimbals. To facilitate spacecraft accommodation, the axes of the mirror gimbal and the axis of the telescope are assumed parallel. In this configuration, the image rotation can be described by [6]

$$\theta = \tan^{-1}(\sin E \tan(A - \pi/4)),$$

where θ is the rotation angle, E is the elevation encoder angle of the mirror and A is the azimuth encoder angle, which is half the angular displacement in ground space. This rotation does not permit all of the footprints to lie parallel to their neighbors, which either results in gaps between footprints or overlapping footprints. Excluding calibrations, overlapping footprints requires 840 steps of a 240 km x 480 km array. The steps become as small as 180 km x 460 km to cover the required area. Not overlapping permits

small, pie-shaped gaps and uses 731 steps of 220 km x 480 km. The difference in number of steps is 13.8%.

The following equation defines a simple metric called "scan efficiency" that can be helpful in understanding the trade space. The "scan efficiency" describes the portion of the hour spent staring at the earth:

$$Scan\,efficiency\,per\,hour = \frac{\frac{Footpr\,\mathrm{int}\,size}{t_{\mathrm{int}}(\,\mathrm{sec}\,)} * \frac{3600\,\mathrm{sec}}{hour}}{\mathrm{Total\,coverage\,area}} \quad ,$$

$$\text{where } t_{\mathrm{int}} = \frac{3600\,\mathrm{sec} - N * t_{step\,settle} - T_{cal}}{N}$$

$$N = \text{number of steps,}$$

$$t_{step\,settle} = \text{step and settle time}$$

$$T_{cal} = \text{total calibration time}$$

The calibration term will be neglected temporarily. For an array footprint size matched to the coverage area with integration time t_{int}= 3600 seconds, the scan efficiency would be very near 1.0 or 100% because the step and settle time is less than 1 second. For smaller array, more footprints on the earth are required for the coverage and the scan efficiency decreases reflecting the additional time spent for N step-and-settle events. Thus not overlapping footprints permits a larger effective footprint size resulting in a smaller number of steps and therefore a longer t_{int} for each footprint. For the specific case described in the paragraph above, not overlapping (permitting gaps) increases the overall efficiency from 60% to 68%, thereby either improving NEDN by <10% and retrievals by <2% or increasing the coverage area by ~ 97 steps (~ 0.6 x CONUS). Table 2-1 describes some of the details of the two scan methods. The release of the draft PORD of June 15, 2001 excludes gaps larger than one pixel in order to form series of images that do not move from one image to the next. Figure 2-1 shows the coverage for the no overlap case.

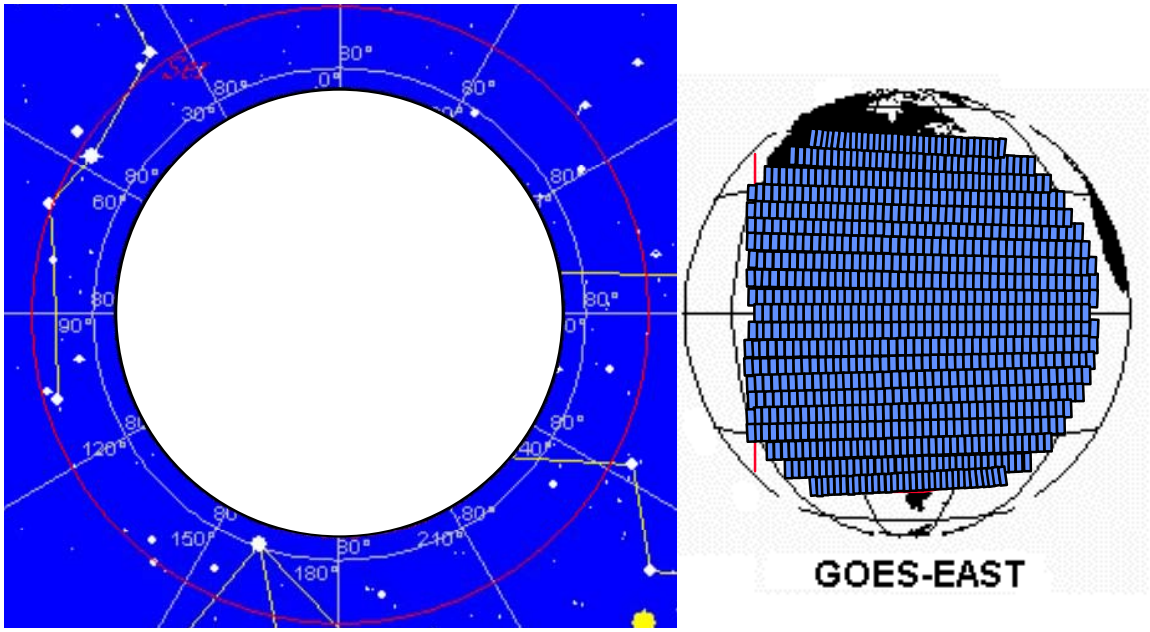

Figure 2-1. The annular region in which star sensing and space views occur is shown at left. The number and location of 480 km x 220 km footprints to provide spatial coverage is shown at right.

2.2.1 Calibration Optimization

Clearly, if all of the time is reserved for measurements, the scan efficiency can be high but the data is uncalibrated. As more time is spent on the calibration to reduce the noise through collection of multiple hot and cold source samples, there is less time available in the hour for Earth observations. Thus it would be beneficial to devise a scan strategy that would optimize the data measurement time while still obtaining adequate calibration.

Neglecting star tracking for now and assuming that the interferogram time is the same for both observations and calibrations, then the total time T_{total} spent making observations is $T_{total}=T_{obs}+T_{cal}$, $T_{cal}=T_{total}*g$, and $T_{obs}=(1-g)*T_{total}$ where g is the fraction below:

$$g = \frac{N_{cals}}{N_{cals} + N_{obs}}, \qquad \text{or} \qquad N_{cals} = \frac{g}{(1-g)} N_{obs},$$

and where N_{cals} is the total number of calibration interferograms, and N_{obs} is the number of observation interferograms. The total number of calibrations is comprised of all of the calibrations performed in one calibration "stop" namely the total of the number of the following: forward-moving mirror hot (blackbody) interferograms, backwards-moving mirror hot (blackbody) interferograms, forward-moving cold (space-look) interferograms and backwards-moving cold (space-look) interferograms.

In our analysis, calibration noise is included in the NEdN, which we define as the precision of the calibrated radiance in each spectral bin. Unlike the current imager and sounder, where calibration errors result in image striping, ABS calibration noise will be very difficult to discern from scene noise because it is a step-and-stare instrument utilizing large detector arrays. With a large area coverage array, the noise produced from scene and calibration acquisitions in any pixel is (ideally) uncorrelated with neighboring pixels. Furthermore, the detector array will not return to the same earth location within a single calibration period. The calibration component of the noise will not change from one array step to the next, but there is little or no consequence to retrieval accuracy. Therefore we include both types of noise in our NEdN estimate.

In Figure 2-2, the standard deviation of the noise variance is plotted versus g with the upper curve representing the result of multiple calibrations using the hot source (upper curve) and on the cold source (lower curve). The noise variances for the cold calibrations, $(\delta I_{cold})^2$, and the hot calibrations, $(\delta I_{hot})^2$, are chosen for the initial cases, $(\delta I_{cold}(0))^2$ and $(\delta I_{hot}(0))^2$, arbitrarily as 0.5 and 1.0 respectively. The variances are of the form

$$(\delta I_{hot})^2=(\delta I_{hot}(0))^2*g(0)/g,$$

$$(\delta I_{cold})^2=(\delta I_{cold}(0))^2*g(0)/g, \text{ and}$$

$$(\delta I_{obs})^2=(\delta I_{obs}(0))^2*(1-g(0))/(1-g).$$

Assuming temporarily that the relative variances in the calibrated radiances are dominated by the variances in the scene flux and the closer signal level (hot or cold), the standard deviations δR are given by:

$$\delta R_{cold} \propto \sqrt{(\delta I_{obs}(0))^2 * \frac{(1-g(0))}{(1-g)} + (\delta I_{cold}(0))^2 * \frac{g(0)}{g}}, \quad \delta R_{hot} \propto \sqrt{(\delta I_{obs}(0))^2 * \frac{(1-g(0))}{(1-g)} + (\delta I_{hot}(0))^2 * \frac{g(0)}{g}}.$$

For only hot scenes, the optimal configuration from this analysis uses 12 sets of calibrations at each calibration stop (the period during which all calibrations are performed. With a minimum of 4 calibrations "stops" during the hour, the 12 sets (hot-forward, hot-backwards, cold-forwards, cold-backwards) of interferograms represent 4 x 48 = 192 calibration interferograms. As shown in Figure 2-2, the fraction g is 0.186 for a total of 840 observation interferograms and 192 calibration interferograms. More

calibrations reduce the total number of observations in the fixed total time for little noise gain. Decreasing the number of calibrations leads to poorer noise performance, assuming that the variance in the scene is dominated by either the hot or cold scene.

Because of both a data rate concern in meeting the 10 Mbps threshold value and a further simulation of radiometric noise (NEdN) sensitivity to calibration source averaging based on scene temperature, the number of cold calibrations was reduced. Initially this reduction changed only the number of observation of the cold blackbody from 12 sets of interferograms to 2 sets of interferograms. However, the result of further analysis that included further scene temperature dependence and determined the variance of the hot, cold, and observed earth scene from simulated spectra using

$$\sigma_H^2 = \frac{\Sigma_M (H_M - \overline{H})^2}{M(M-1)}, \quad \sigma_C^2 = \frac{\Sigma_{M'} (C_{M'} - \overline{C})^2}{M'(M'-1)}, \quad \sigma_{obs}^2 = \frac{\Sigma_{M''} (Obs_M - \overline{Obs})^2}{M''(M''-1)},$$

the required number of cold calibrations increased, which decreased the number of hot calibrations. With the data rate constrained and allowing for the coldest earth scenes, the expression for NEDN below yields 6 sets of forward and backwards hot interferograms and 6 forward and backwards cold interferograms:

$$NEDN^2 = \frac{(R_{hot} - R_{obs})^2}{(\overline{H} - \overline{C})^2}\left[\sigma_{obs}^2 + \sigma_{hot}^2 \gamma^2 + \sigma_{cold}^2 (1-\gamma)^2\right] \quad \gamma = \frac{(E - \overline{C})}{(\overline{H} - \overline{C})}.$$

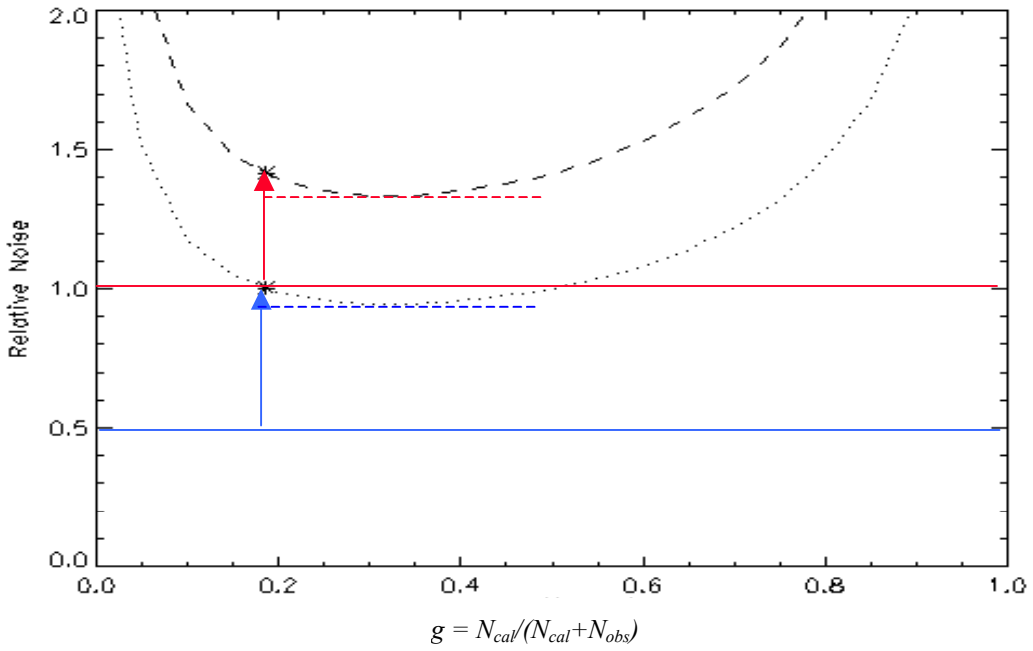

Figure 2-2. For a fixed number of observations and a fixed integration time for all interferograms at each g-value, the noise associated with warm (top) and cold (bottom) calibration interferograms is parameterized against the ratio of the number of calibration interferograms to the sum of the number of calibration and observation interferograms.

Figure 2-3 shows that the calibrated NEdN depends on the scene flux, which is parameterized here as an equivalent blackbody temperature. There is little or no benefit in including many averages of the cold source in the calibration procedure [7], particularly when the instrument is viewing warm scenes. For cold scenes however, there is some reduction in NEDN when the cold calibrations are included. Because the atmospheric spectra resulting from the interferogram covers both warm and cold observations in various portions of the wavelength scale, each spectra contains both warm and cold scenes, necessitating the use of both the hot and cold calibration data.

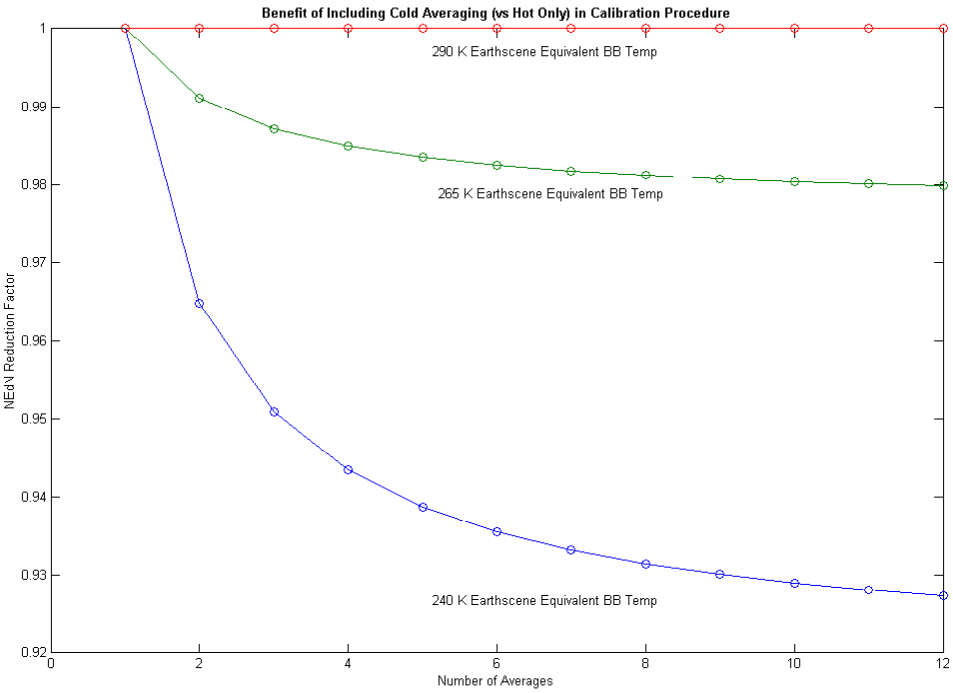

Figure 2-3. NEdN reduction factor, assuming a fixed interferogram dwell time, when including equal numbers of both hot and cold source averages in the calibration procedure as opposed to only averaging the hot source data.

Four calibrations stops in the hour constrain the focal plane drift [8]. In order to provide more frequent calibrations to account for solar heating, 5 calibration stops have been scheduled. However, a maximum of 6 calibrations stops per hour is possible when necessitated by rapidly changing spacecraft conditions associated with solar heating, and when using only the previous discussed 6 sets of blackbody calibrations. Any additional calibration stops during eclipse will be the result of easing the coverage rate during eclipse, as described in the draft PORD of June 15, 2001.

ABS operations resulting from this scan scenario are detailed in Table 2-1. In that table, the combined effect of the calibration and star-sensing overhead (discussed below) is used along with an estimated 0.24 second slew-and-settle time between interferogram acquisitions to determine the overall scan efficiency of the ABS point design. Figure 2-4 and Figure 2-5 show the overlap scan plan and the no overlap scan plan, respectively. The star tracking and calibration are noted pictorially.

2.2.2 Star Sensing Observations

Star sensing operations must be included in the 1 hour allowed for spatial coverage. In order to maximize the time for the 8 star-tracking observations during the hour, the 4 calibrations (6 maximum) will occur during the star tracking observations.

Historically 4th magnitude, or brighter, stars have been used in these operations, however this necessitates that scan operations be interrupted when such a star is available for viewing. By extending to 7th magnitude, it is possible to ensure that an appropriate star will be available when necessary, with no need to interrupt acquisition of an E-W swath of footprints, thus minimizing overhead. Using a star database and the GOES East view, it was possible to determine that a 25 degree field of regard (FOR) defined by a round baffle would be required to provide enough stars to prevent interruption of a row of data. This corresponds to an annulus 3.85^{o} wide surrounding the Earth. Stars of 7th magnitude can be sensed using a low-light visible channel when sunlight is outside of the 25 degree FOR. Star sensing and visible channel detector performance are discussed in Section 2.5.3.

The total integration time was determined by allocating time within the hour for Earth scene measurements, instrument calibration, and star tracking. In order to minimize the time spent moving to a star, no interruptions of a row were permitted for star tracking. For the overlapping scan coverage, the integration time was 3.0 seconds. Table 2-1 details the combined effect of the calibration and star-sensing overhead, while Figure 2-4 and Figure 2-5 note the star tracking pictorially.

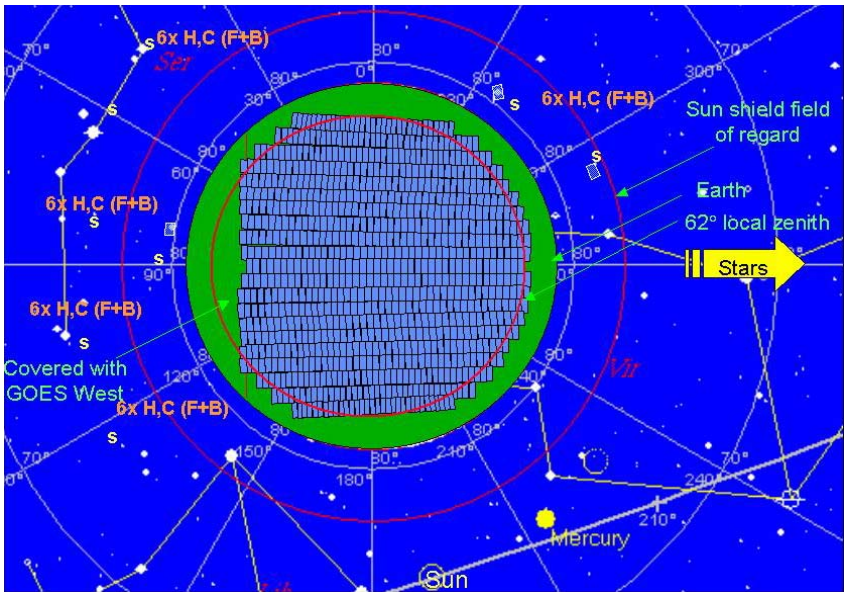

Figure 2-4. Overlap scan plan (25º annulus=17.3º for earth+7.7º for stars) with 7th magnitude stars.

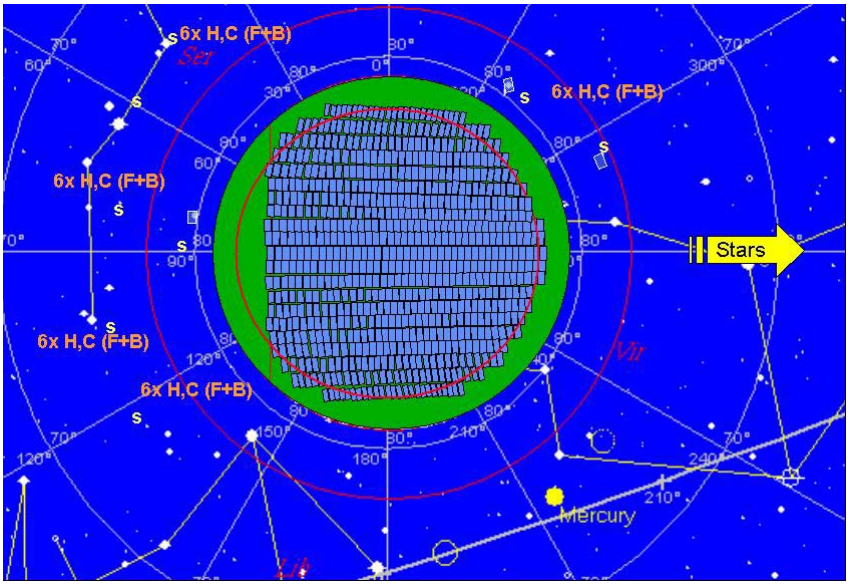

Figure 2-5. No overlap ("gap") scan plan (25º annulus=17.3º for earth+7.7º for stars) with 7th magnitude stars.

Table 2-1. Scan Parameters

Property	Overlapped footprints	Non-overlapped footprints
Number of rows	21	21
Steps per row	46 (longest, 2.5 min), 32 (shortest)	39 (longest, 2.4 min), 25 (shortest)
Maximum gap	N/A	4 pixels E-W, >1 pixel N-S
Stare time per step	3.0 s	3.4 s
Total number of steps	840	731
Calibration stops	24 interferograms (6 cold forward and backward sweep / 6 warm, forward- and backward-sweep)	24 interferograms (6 cold forward and backward sweep / 6 warm, forward- and backward-sweep)
CONUS coverage time (est.)	12.7 min.	13.0 min.

2.3 Optical Subsystems

The point design optical system comprises a scan mirror, an unobscured afocal telescope, two visible optical channels with 1-km resolution, and three infrared optical channels with 10-km resolution. The three-mirror afocal telescope is designed for a 530 x 500 km field-of-view. Following the telescope, a dichroic beamsplitter reflects the visible radiation and transmits the infrared radiation. Two visible channels provide cloud sensing and low-light imaging capabilities. The required portion of each CCD covers a 480 x 220 km portion of the 530 x 500 km visible channel field-of-view. The telescope delivers a 3.3 cm collimated IR beam to the Michelson interferometer, which has a full sweep of 0.8 cm, providing the necessary spectral resolution. Field-imaging catadioptric aft optics operating at *f*/0.85 provide a 530 x 250 km field-of-view to three IR focal planes (the arrays, described in Section 2.5.1, populate a 480 x 220 km portion of this field).

2.3.1 Scan Mirror

The point design has a 30.5 cm (12 inch) aperture diameter, which led to scan mirror dimensions of approximately 33.5 x 47.5 cm. The baseline design makes use of a silicon carbide (SiC) scan mirror, lightweighted by 50%. A layer of silicon serves as a polishing surface. This construction mitigates past problems with mirror deformation under solar heating because the ratio of stiffness to the coefficient of thermal expansion (CTE) is much higher for SiC than for beryllium. A reflective coating of aluminum with a protective overcoating of yttrium oxide (Y_2O_3) is assumed for the baseline [9] in order to avoid calibration difficulties [10] arising from angle-dependent mirror emissivity. The emissivity variation over the $45^o \pm 5^o$angular range of the scan mirror of the current SiO_x scan mirror coating and the point design coating is shown in Figure 2-6.

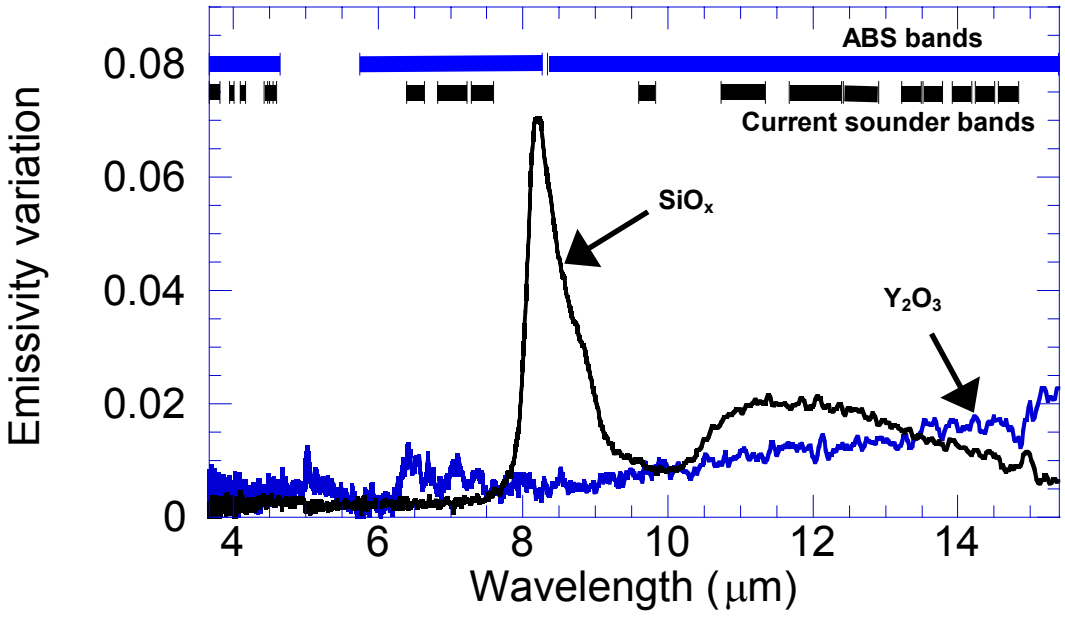

Figure 2-6. The angular emissivity variation of the existing and point-design scan mirror coatings. The spectral coverage of the existing sounder and ABS is shown as a horizontal bar.

2.3.2 Input Telescope Optics

The input telescope has a 30.5 cm collecting aperture and produces a 3.3 cm collimated output. The afocal telescope comprises three powered mirrors, the primary and secondary sharing a common axis of symmetry, the tertiary tilted to allow access to the intermediate image with the increased optical field. An off-axis section of each mirror is used. The image of the aperture stop was placed near the scan mirror to minimize the required size of the scan mirror. Because the entrance pupil is also near the calibration source, the regions of the source viewed by individual detectors overlap significantly. Each detector views approximately a 30.5-cm diameter region of the calibration source. For this design, the linear shift of the areas on the calibration source viewed by the various detectors is only a few percent. An accessible field image in the input telescope provides a convenient location for an internal stop that can be used to reject out-of-field radiation. This, along with the off-axis design, helps minimize problems associated with stray light when viewing regions of the Earth that are in close proximity to the Sun during eclipse periods. An illustration of the point design input telescope is shown in Figure 2-7. Other input telescopes that occupy smaller volumes but cover less optical field are discussed as part of spacecraft accommodation in Section 2.9.

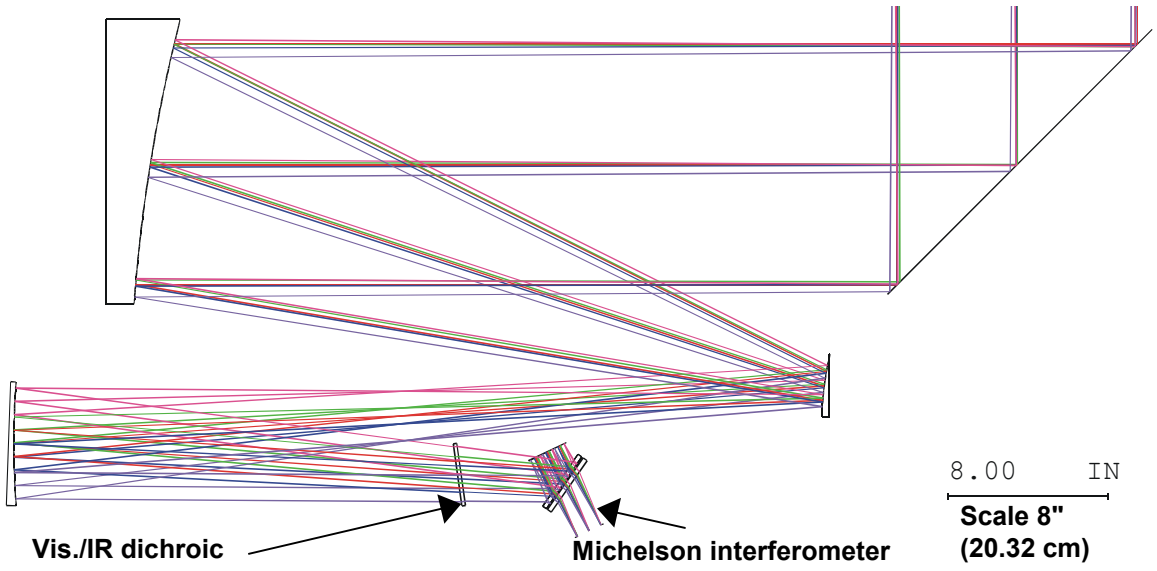

Figure 2-7. The ray-trace of the input telescope.

2.3.3 Interferometer and Metrology

The Michelson interferometer accepts the 3.3 cm collimated beam produced by the input telescope. As configured for this point design, only a 530 x 250 km portion of the telescope field-of-view can be transmitted through the interferometer without vignetting. The moving mirror on the interferometer has a full physical sweep of 0.8 cm, producing a 1.6 cm maximum OPD ($\pm$ 0.8 cm OPD). The field-of-view within the interferometer is 8.7-degrees corner to corner for the 530 x 250 km ground FOV and 7.8 degrees corner to corner for the 480 x 220-km portion of the FOV covered by the detectors.

A zinc selenide (ZnSe) beamsplitter / compensator pair was selected based on the considerations (throughput at 15.1 μm and mechanical properties) outlined in the trade of Section 4.3.3 of Reference 2. A ray-trace diagram of the interferometer is shown in Figure 2-8.

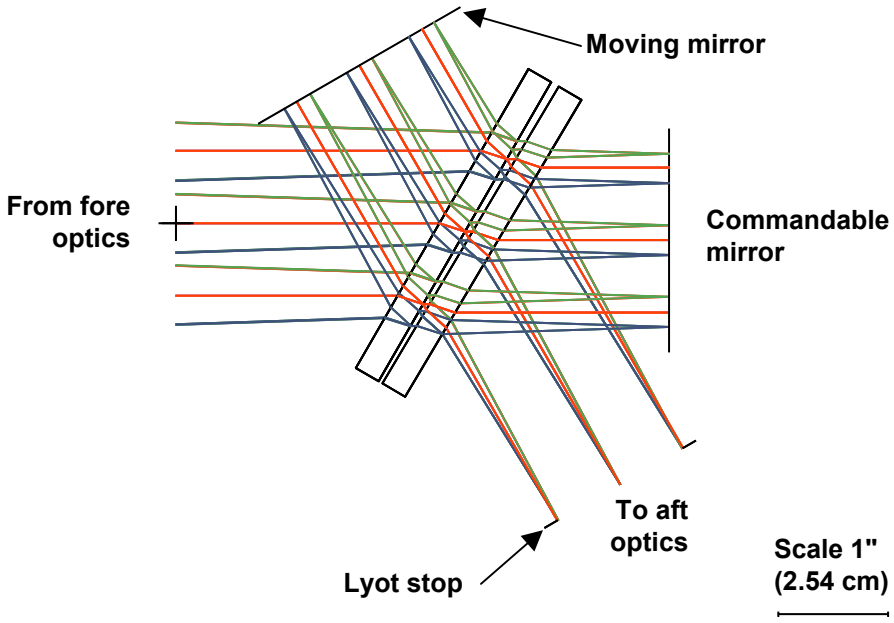

Figure 2-8. The ABS interferometer, highlighting the position of the Lyot stop.

The metrology optics are illustrated schematically in Figure 2-9. The metrology beam and the infrared signal beam use the same interferometer components to assure that both will have the same optical path difference during the stroke of the moving mirror. To avoid introducing a central obscuration into the system, the metrology beam is injected into the interferometer using turning flats which are located above the infrared beam path.

The details of the standard metrology operation are explained in Section 3.5.2 of Reference 2, but may be summarized by recognizing that the two passes through the eighth-wave plate in one arm of the interferometer generate circularly polarized light in that arm. The signal at the metrology in-phase and quadrature (I and Q) detectors is produced by interference between the linearly and circularly polarized light from the two arms of the interferometer. More information on the metrology sampling is located in Section 2.7.2.

A beamsplitter is used to introduce a second metrology beam that can be used to monitor tilt of the moving mirror, which may occur as the mirror moves through its stroke. The second metrology beam, located below the first metrology beam and above the infrared beam, is detected by an InGaAs array. Tilt is determined by using on-board processing to analyze the intensity variations in the interference pattern.

If it is anticipated that a more precise tilt determination than that described in Section 2.7.2 is required and the higher power laser is not obtainable, additional metrology beams with single element detectors located around the perimeter of the signal beam can be considered. The tilt information could then be obtained from these detectors through the use of phase detection electronics.

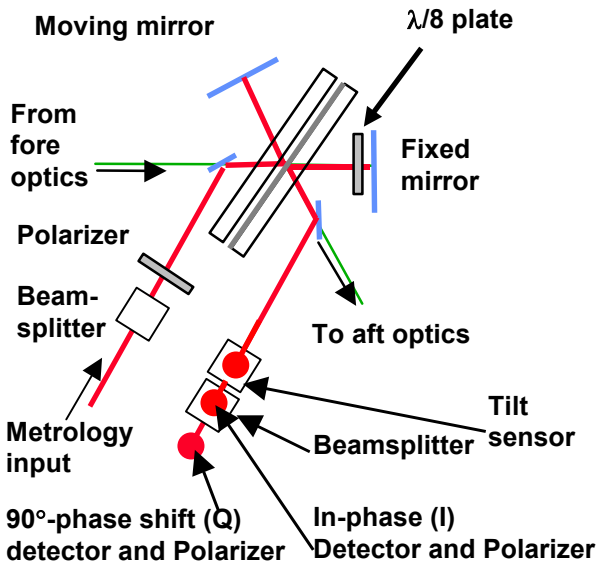

Figure 2-9. The arrangement of the metrology optics, along with the IR FPA sampling.

2.3.4 Aft Optics

The trade studies of Section 4.3.6 of Reference 2 were not re-evaluated because the assumed use of photovoltaic (PV) HgCdTe detector arrays retained a preference for field-imaging aft optics. The

catadioptric design remains a good choice since each channel has an internal image formed by the common reflective components and these images can be used to improve coregistration. Obtaining a wide field while operating at *f*/0.85 proved to be a substantial challenge, however, thus an optical design giving a 530 x 250 km field was formulated. This field permits some upgradeability to IR FPA's larger than the 48 x 22 array baseline covering the 480 x 220 km FOV. The aft optics are shown in Figure 2-10.

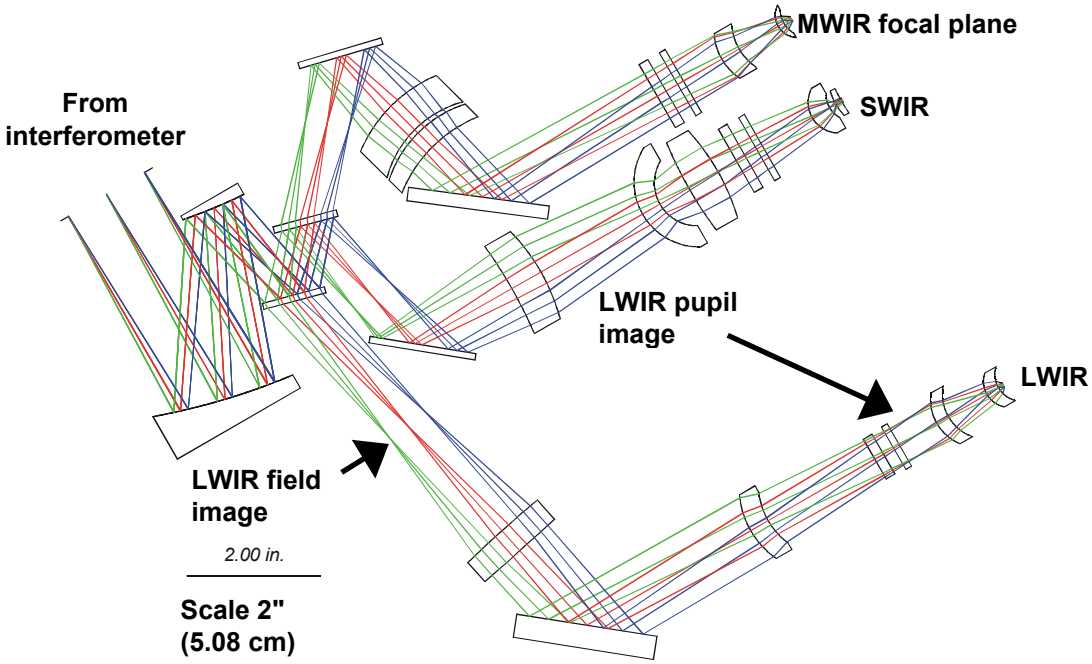

Figure 2-10. The ABS aft optics design, illustrating the three IR wavebands.

2.3.5 Visible Optics

A refractive *f*/1.4 optical system was used for the baseline. It provides a 530 x 500 km field-of-view (twice that of the IR optics). Although this field is not fully populated because the baseline CCD footprint has been chosen to match the 480 x 220 km IR FPA footprint, sufficient field exists for a visible field ground footprint twice as large as the infrared ground footprint. Details are provided in Section 2.5. The visible optics are shown in Figure 2-11.

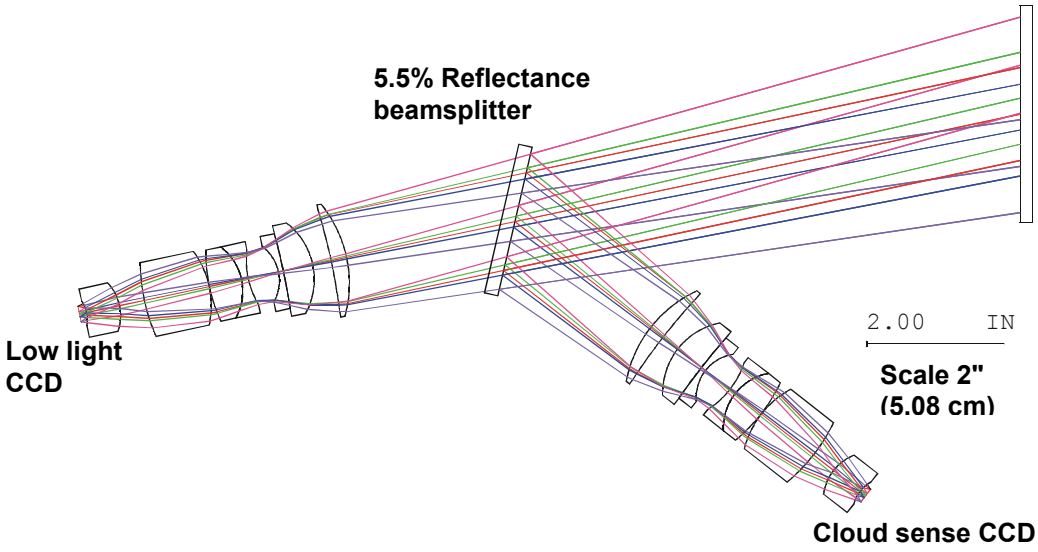

Figure 2-11. The ABS visible channel design.

2.4 OPTICAL PERFORMANCE

Infrared optical performance. Figure 2-12 displays the spot diagrams for each of the three infrared channels. The on-axis field point, a point on the corner of the detector-populated field-of-view and a point on the corner of the maximum field-of-view for which the system was designed are shown. The squares surrounding each spot diagram represent the 60-μm square active pixel area and the 72-μm pixel pitch. The circles associated with each spot diagram indicate the diameter of the first null of the Airy disk at the two extremes of the waveband. Review of Figure 2-12 shows that the geometrical spot size in all cases is significantly smaller than the active pixel area. Because of the fast optical system, the diffraction spot diameters are also significantly smaller than the active pixel area. The small geometrical spot and the small diffraction spot are necessary if one is to meet the ensquared energy requirement that at least 90% of the response detected in a sample must originate from a 10 x 10 km ground sample corresponding to this FOV.

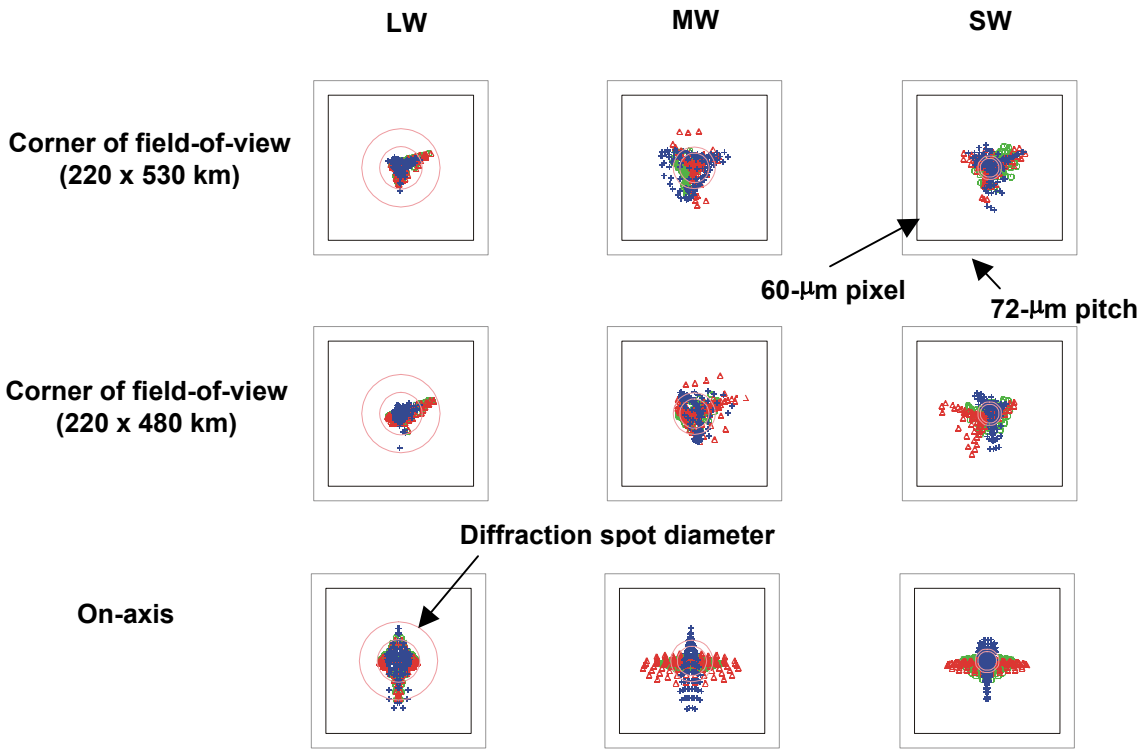

Figure 2-12. Spot diagrams for the infrared channels.

Visible optical performance. Figure 2-13 displays the spot diagrams for the visible channel. The on-axis field point, a point on the corner of the detector-populated field-of-view and a point on the corner of the maximum field-of-view for which the system was designed are shown. The square associated with each spot diagram represents the 12-µm square pixel dimension. The visible optical system is not diffraction-limited. The geometrical spots are matched to the pixel dimensions. The visible system is designed for a waveband from 500 to 700 nm, which provides good performance over the 520 to 720 nm visible band. The different characters on the spot diagrams indicate that there is residual chromatic aberration in the system.

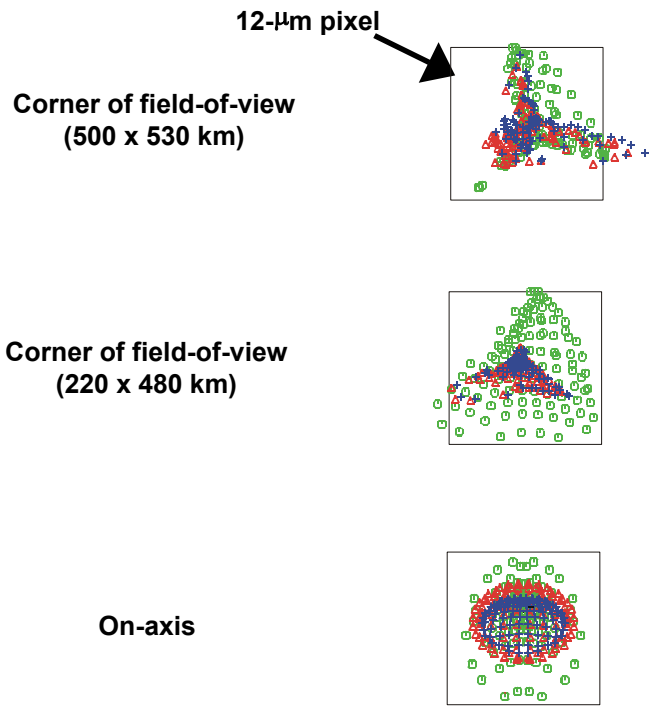

Figure 2-13. Spot diagrams for the visible channel.

The performance of the infrared channel, along with the diffraction characteristics of the instrument, determines the immunity of observations from contamination by adjacent or nearby observations. This topic was treated extensively in Reference 3; indeed, it motivated that work. The 90% ensquared energy requirement in the January 2001 TRD is used to address this need for immunity from contamination by nearby clouds. Figure 2-14 illustrates that this requirement is met by the point design in all three IR bands. Two curves are shown. The lower curve gives the percent of the detected energy that falls on the central pixel for 72-μm pixels on 72-μm pitch. For these abutting pixels, all energy is detected. This curve illustrates that only the SWIR channel would meet the January 2001 TRD requirement. The upper curve gives the percent of the detected energy that falls on the central pixel for 60-μm pixels on 72-μm

pitch. Energy that falls into the gaps between the pixels is not detected. This energy loss is accounted for in the NEdN calculations. The upper curve illustrates the advantage of undersizing the pixels and shows that with this detector configuration all three channels meet the January 2001 TRD requirement.

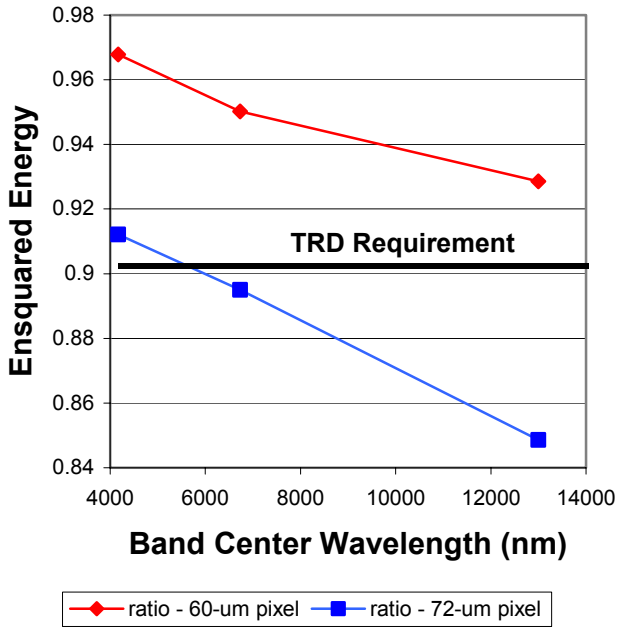

Figure 2-14. Ensquared energy performance of the ABS point design (pixels on 72μm pitch).

2.5 Detector Point Design

This section briefly summarizes the detector configuration chosen for the ABS point design. The original work documented in Reference 2 included several sections (4.4, 4.5, 4.6, and 4.8) that evaluated detector options for an FTS-based sounding instrument. The fundamental conclusions remain largely unchanged in this work, although there is a general move toward larger and colder IR arrays to provide the enhanced coverage rate and NEdN required of this point design. All three IR arrays are assumed to operate at 65 K for the sake of simplicity and because the switch to active cooling provides ample margin. This is a major difference from the work in Reference 2. All three IR detector arrays operate in the background-limited photodetection (BLIP) condition, maximizing sensitivity. In the case of the visible CCD, most original

assumptions remain valid except that two CCD's are now present, one that is dedicated to low-light imaging and star sensing which receives most visible flux, and a second that is used for cloud sensing.

One notable aspect of this point design is that the optical field is not fully utilized by either the visible or IR focal planes. In the case of the IR focal planes, constraints relating to the number of LWIR output taps and well capacity led to the selection of a 220 x 480 km SSP array footprint (22 x 48 pixel array format) versus the 260 x 530 km field produced by the system optics. This approach of not fully utilizing the optical field also simplified the sensor design by minimizing the raw data rate, while still meeting performance requirements. It also provides an upgrade path should larger arrays (or larger data rates) become less technologically stressing. In the case of the visible CCDs, the used field is chosen to match that of the IR arrays, whereas the optical system provides a 500 x 530 km field.

2.5.1 Infrared Detector Configuration

The assumed use of PV $Hg_{1-x}Cd_xTe$ IR focal plane arrays remains unchanged from Section 4.4 of Reference 2. Likewise, the 15.1-μm cutoff wavelength for the longwave IR array remains the same from Section 4.5 of the earlier study. Because both the model and the retrievals have undergone modifications since the original ABS study, a few cases of the cutoff wavelength study of the original report were rerun to validate the performance at 65 K. In order to study the dependence of the cutoff wavelength on the retrieval results, the Cd concentration was tuned with a fixed temperature to produce NEdN values for peak responsivities at λ_{peak} = 13.0, 13.3, and 13.7 μm. Each of these data points represents a separate case, and in each case the noise performance was recalculated and the covariance matrix was recomputed. We are using a common definition of the peak responsivity, namely that the peak wavelength is 10 percent shorter than the defined cutoff wavelength. Figure 2-15 shows that at 65 K the 1 K NWS threshold performance is best met with the 13.7 μm peak detector, which has a cutoff wavelength of approximately 15.1 μm. Figure 2-16 shows the relative humidity plot, which is not sensitive to LWIR detector doping.

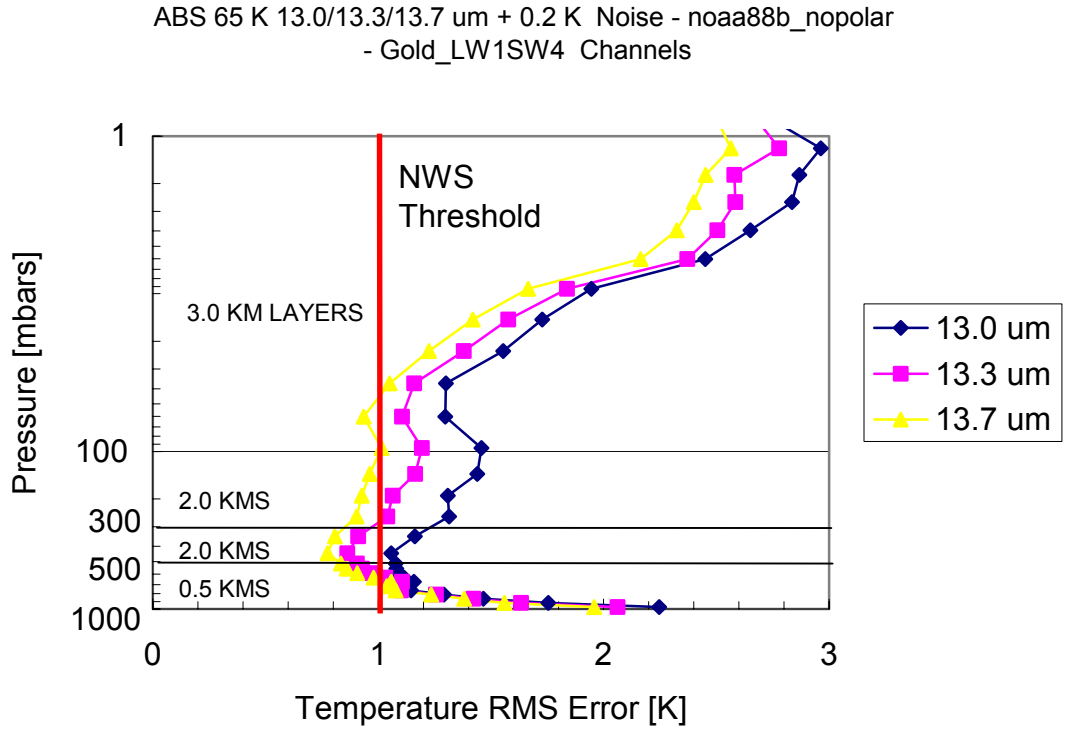

Figure 2-15. Retrieved temperature performance as a function of detector cutoff wavelength, updated for the latest interferometer performance model and retrieval assumptions.

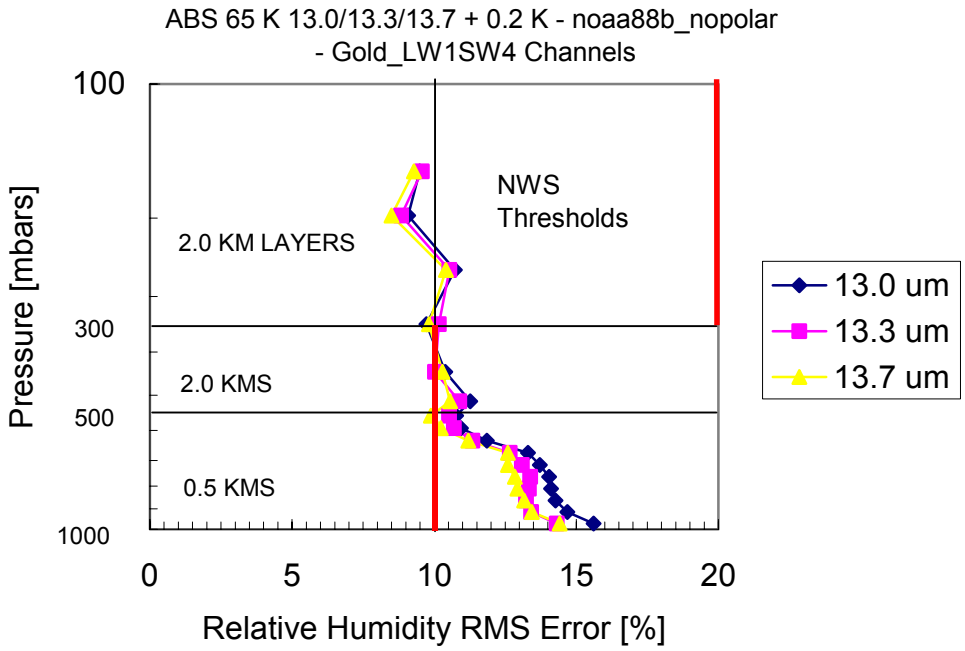

Figure 2-16. Retrieved relative humidity performance as a function of detector cutoff wavelength updated for the latest interferometer performance model and retrieval assumptions.

Table 2-2. Summary of IR Detector Focal Planes

Property	SW Band	MW Band	LW Band
Cutoff wavelength at 65 K (μm)	4.7	8.5	15.1
Pixel size (square geometry)	60 μm active area on 72 μm pitch	60 μm active area on 72 μm pitch	60 μm active area on 72 μm pitch
Array size (long axis aligned to N-S)	22 x 48	22 x 48	22 x 48
Quantum efficiency	97	75	62
Responsivity (A/W)	3.33	4.70	6.85
R_0A (Ω-cm^2) at 65 K	>1 x 10^6	>1 x 10^5	38
D* (cm $\sqrt{Hz}$ / W) at 65 K	8.81 x 10^{11}	2.56 x 10^{11}	1.48 x 10^{11}
Charge storage (e^-)	3.8 x 10^8	1.55 x 10^8	3.75 x 10^8
Number of outputs and readout rate	1, 7.3 MHz	8, 450 KHz	16, 450 KHz
Type of preamplifier	Capacitive transimpedance amplifier (CTIA)	Buffered direct injection (BDI)	BDI
Read noise (μV) **(**See Figure 2-18)	380	95	95
Estimated operability	**TBD**	**TBD**	92%(See Figure 2-19)
Power dissipation	~140 mW	~90 mW	~140 mW

The IR focal plane arrays are summarized in Table 2-2. The numbers quoted are median values for the arrays. The IR focal plane arrays are unique in several respects. The pixel geometry deliberately reduces the fill-factor in order to improve the ensquared energy (derived from Reference 3 and MTF measurements performed in house). The active area of the detector is 58 μm square separated from adjacent pixels by 72 μm, shown in Figure 2-17. The boundary of each detector may be achieved by masking or etching a contiguous array, or by selectively implanting diodes, presumably with little consequence to the noise performance. Modeled instrument performance assumes no degradation from these measures.

The readout integrated circuit is also a unique feature of the IR focal plane array design, particularly in the LW band. The capacitors, which integrate charge in each preamplifier, are not physically located in the silicon below each pixel. Instead they are located in the periphery of the array and coupled to the detector element through trace wires. Manufacturing limitations on the minimum trace width is approximately 3 μm. For a 72-μm pixel pitch, the array can have at most 24 traces leading from each side of the detector array. Each signal trace is paired with a grounded trace so that the 22-pixel (E-W) format is near the maximum allowable size. The use of large periphery capacitors avoids the need to read the array out at high speeds, and reduces the raw data rate. The large signal anticipated can be integrated for up to 145 μs compared to about 90 μs if the capacitor area is constrained by the pixel dimension. This architecture also enables the use of a 1.5 μm laser for metrology, and 0.5 MHz 16 bit analog-to-digital converters (discussed in section 2.7.2).

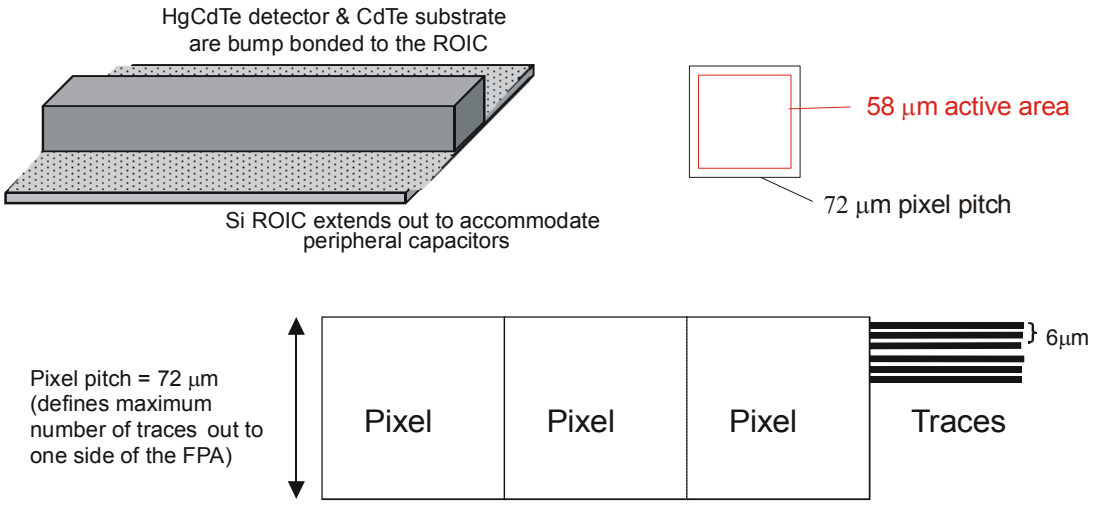

Figure 2-17. FPA Architecture

The use of a capacitive transimpedance amplifier (CTIA) architecture for the pixel preamplifier is retained in the SW band from Reference 2. The use of buffered direct-injection (BDI) preamplifiers is assumed in the MW and LW bands. BDI preamplifiers afford most of the benefits of the CTIA and more easily accommodate a capacitor located in the periphery of the ROIC. Small signal problems associated with BDI designs will be avoided in the MW and LW because of the large background flux present.

During the design of the IR focal plane arrays, an effort was made to minimize the readout rate in order to keep the read noise low compared to the detector noise. It can be shown that the read noise contribution to the system NEdN is proportional to a constant noise density, tap rate, sample integration time, preamplifier capacitance, and interferogram length by:

$$NEdN_{readout} \propto e_n \frac{\sqrt{f_{Tap}}}{\sqrt{N_s}} \frac{C}{\tau}$$

where e_n is the noise voltage density (Volts/sqrt(Hz)), f_{tap} is the readout tap rate (Hz), C is the preamplifier capacitance (farad), τ is the sample integration time, and N_s is the number of interferogram samples.

The capacitors are sized to be large enough to accommodate the integration time with about 15% margin to avoid non-linear effects that occur near full well. The number of samples is determined from the sample integration time, interferogram dwell time, and duty cycle. Following the above equation, the use of multiple outputs (16 for the LWIR band, 8 for the MWIR band) is required in order to meet the January 2001 TRD NEdN threshold. The baseline performance of the readout is somewhat aggressive, but is within, the typical limits [11] of like devices. Figure 2-18 shows typical limits plotted with a sampling of similar focal plane array readouts (acquired from data sheets, journal articles, private communications, and in-house measurements).

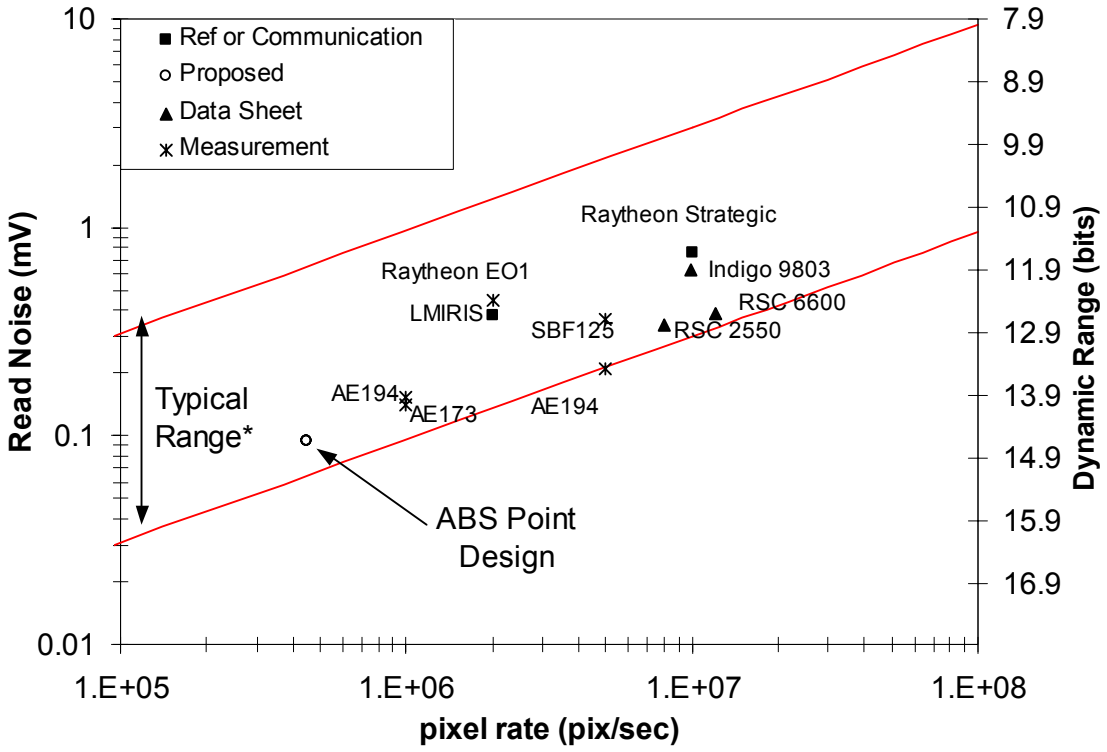

Figure 2-18. The read noise of several demonstrated longwave FPA's, along with typical bounds of performance as a function of data rate.

A second crucial issue is that the ABS point design marks the first use of large two-dimensional staring detector arrays in GOES instruments. Because an FTS is incompatible with continuously scanned operation, the presence of ground FOV dropouts arising from detector outages is unavoidable. A tradeoff must be made between detector operability (the percentage of valid FOV soundings in an area) and procurement cost and risk. It is felt that a reasonable standard for "operable" detector pixels is those that are within a factor of two of the median detector performance. Figure 2-19 illustrates the detector-limited NEdN on an ABS-like LWIR array measured at MIT/LL. Approximately 92% of the detectors meet the above operability criterion. Note that no operability requirement is present in the NESDIS January 2001 TRD, but there is clearly a need to maximize this parameter. Dithering (e.g., by a few rows or columns) of the coverage region between subsequent frames can be used to eliminate the repeated loss of data from any ground FOV arising from a non-operable detector.

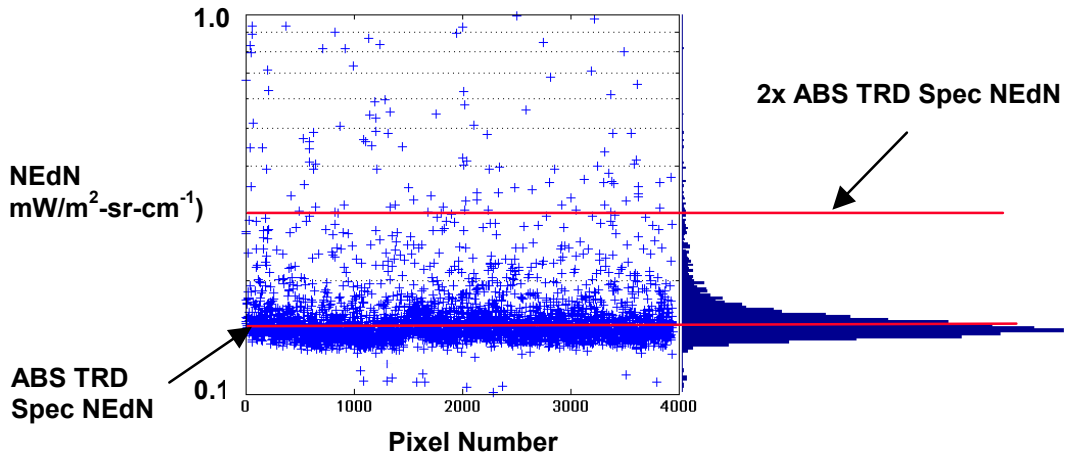

Figure 2-19. Likely LWIR array NEdN statistics based on laboratory measurements of HgCdTe longwave focal plane arrays. Approximately 92% of pixels are within twice the NEdN threshold.

2.5.2 Infrared Detector Operation

Over the past several years, a detailed radiometric model has been developed at MIT/LL to evaluate the performance of FTS instruments. The model is intended to provide a reasonable estimate of instrument performance. It has evolved with instrument complexity since it was first developed on the ITS program. [12] Various components of the model have been validated [13] through comparisons with flight data from operational instruments. The model predicts the attainable performance of an atmospheric sounding instrument such as ABS with a reasonably high degree of confidence. In conjunction with the wide-field optical design of Section 2.3, the 65 K operating temperature achieved through active cooling, and reasonable assumptions concerning interferometer performance and signal processing, this model predicts that a number of detector operating conditions can be adjusted to meet the NEdN requirements. The optical design was combined with the assumptions of Table 2-3 to calculate the background photon flux and scene photon flux on the detectors. Note that the term "transmittance" is used in place of reflectance for mirrors.

Table 2-3. ABS optics conditions assumed in background calculations.

Component type	Temperature (K)	Emissivity	Transmittance Per Component
Ambient reflective optics	295-318	0.05	0.95
Cold reflective optics	200	0.05	0.95
Ambient dichroic (vis/IR)	295	0.1	0.88
Cold dichroics	200	0.1	0.82
Beamsplitter/compensator	200	0.1	0.35
Cold refractive optics	200	0.005	0.95
Filters*	<80	0.05	0.85

* Emission from filters was assumed to have a maximum wavenumber of 5000 cm^{-1} and a minimum wavenumber defined by the appropriate band (SWIR/MWIR/LWIR). Radiometric calculations for other elements used the minimum and maximum wavenumbers of the appropriate band.

The detector operating conditions derived from using the radiometric model to verify compliance with January 2001 TRD NEdN requirements are summarized in Table 2-4.

Table 2-4. Assumed ABS detector operating conditions.

Parameter	SWIR band	MWIR band	LWIR band
Spectral band (cm^{-1})	2150 - 2720	1210 - 1740	650 - 1200
Spectral resolution (cm^{-1})	2.5	1.25	0.625
Dwell time (s)	3.0	3.0	3.0
Sampling (frame) rate (Hz)	6900	3450	6900
Integration time (μs)	145	290	145
Average Photon flux ($q/(cm^2\ s)$)	2.4×10^{14}	8.7×10^{15}	6.3×10^{16}
Quantum efficiency	0.97	0.75	0.62
NEdT (K), with 250 K blackbody and *f*-cone matched optical design operating at peak responsivity wavelength [290 K Scene]	0.40 at 2250 cm^{-1}	0.12 at 1350 cm^{-1}	0.11 at 800 cm^{-1}
NEdN ($W/(cm^2\ sr\ cm^{-1})$) [290 K Scene]	0.01 at 2250 cm^{-1}	0.05 at 1350 cm^{-1}	0.13 at 800 cm^{-1}

The LWIR integration time corresponds to the maximum that is available given the charge storage capacity, assuming a 15% margin for linearity considerations. The dwell time during which the interferogram is obtained satisfies the coverage requirement when used with the 22 x 48 array format, including necessary calibration and star sensing overhead. The LWIR interferogram is sampled twice for each fringe of the 1.5 μm metrology laser by counting I and Q zero-crossings. The MWIR band is sampled once per fringe, doubling the integration time. The SWIR interferogram is sampled at the same

rate as the LWIR. The LWIR interferogram is sampled between ±0.8 cm OPD. The MWIR interferogram is sampled between between ±0.4 cm OPD, halving the spectral resolution. The SW is sampled between ±0.2 cm OPD, cutting the spectral resolution by four over the LWIR band. Processing of sampled interferograms is described in Section 2.7.3.

2.5.3 Visible Detectors: Configuration and Operation

The visible detectors are assumed to be a commercially available 1024 x 1024 pixel silicon frame-transfer CCD array, with only a portion of the array utilized. This portion is a minimum of 220 km x 480 km subframe. Because the time to quickly shift the accumulated charge across the utilized portion of the CCD into the frame transfer buffer is not negligible compared to the integration time for earth scene levels, it was necessary to use a beamsplitter coated 94.5%/5.5% to shunt the majority of the signal (a factor of 18) away from the full-albedo (cloud-clearing) CCD. This particular choice permits a longer earth-scene integration, which makes the shift time about one tenth of the integration time, while avoiding mechanisms such as mechanical shutters or choppers that may fail. The visible detector focal planes (two identical CCD's are assumed) are summarized in Table 2-5.

Table 2-5. Summary of visible detector focal planes.

Property	Full-albedo and low-light CCDs
Pixel size	12 μm
Array size	480 x 220 minimum
Frame transfer shift time for 220 pixels	0.36ms
Frame rate	~ 30 Hz
Quantum efficiency	0.30 minimum
Charge storage (e^- / pixel) (linear region)	300,000
Read noise (e^- / pixel)	18
Dark current at 300 K (TE stabilized) (e^- / (pixel s))	225

The full-albedo CCD is dedicated to daytime cloud sensing (star sensing operations are described in Section 2.2.2). At the nominal 1 km visible FOV, the full-albedo visible channel gives an expected SNR of 548 assuming a 3 ms integration. The overall optical throughput of 2.4% up to the surface of the detector for this channel provides the necessary flux reduction during the integration period. This assumes 95% reflection for each of the surfaces of the scan mirror and telescope, 88% transmission for the visible/IR dichroic, 98% for each of the lenses, 75% for the visible filter, and 5.5 percent reflection for the visible splitter.

Star sensing with a CCD represents a departure from the current GOES star sensing technique described in Reference 2. The CCD will be positioned so that its center images the expected star position. The distance from the center of the array to the image of the star then provides the measure of the deviation of the mirror. Because the motion of the star (72 μrad/sec) will cause its image to drift during the image collection, a streak over two pixels will be formed on the CCD. Centroiding will thus be required to determine the center of the star location to better than 1 km. The modeled performance for a 4th magnitude star of class B0 gives S/N=158 for 1-second integration, while the performance for a 7th magnitude star during a 1- second integration gives S/N=34. A class M0 star gives about half of the flux of the B0 star. When compared to signal-to-noise values for the current GOES star tracking, there is margin of a factor of three in the 7th magnitude integration time that permit end-of-life operation.

During eclipse, sunlight will impinge on the surface of the scan mirror, causing scattering, while the sun is both in the FOV and not eclipsed by the earth. However, the worst-case scenario of star sensing with the rays of the sun impinging on the scan mirrors at nearly the same angle as the star's rays need not be chosen because star sensing can be performed elsewhere in the FOV of the sunshield. The sun will cross from the edge of the sun shield FOV to the limb of the earth during a 15.4-minute period. Thus the small number of calibrations taken during this period, nominally one ore two, can be performed as far away as possible in the FOV from the sun. In this scenario, the forward scattering will miss the first mirror of the telescope and hit an optical baffle, with only the low level signal increase from surface irregularities making to the telescope primary. In this case the star sensing will require use of a star with a magnitude of 4 or brighter.

In order to support the January 2001 TRD "goal" of low-light imaging capability, a second identical CCD dedicated to low-light imaging is in the 94.5% transmitted path of this beamsplitter. This CCD is allowed to saturate in daylit portions of the Earth scene where it is not in use. A number of options are available to incorporate low-light imaging at useful signal-to-noise ratios. The corresponding performance for the low-light channel, which has an overall optical throughput of 43% up to the detector, depends on incident illumination level. Pixels can be aggregated, or binned, to improve performance; however, at the lowest light levels the performance is limited to a binary yes/no detection. The low-light imaging performance of the ABS point design is summarized in Table 2-6.

Table 2-6. Low-light imaging channel performance.

Illumination		SNR at 1 km resolution	SNR at 5 km resolution
Full moon		115	530
Quarter moon		29	158
Twilight	Sunset (sun at 0°)	540	N/A
	Civil twilight (sun at -6°)	221	N/A
	Nautical twilight (sun at -12°)	13	77
	Astronomical twilight (sun at -18°)	1	8

2.6 Mechanical And Thermal Design

The mechanical concept of this ABS point design is very similar to that of Reference 2. Differences in the mechanical design of this point design from those of Reference 2 arise primarily from the following considerations:

1. A larger aperture diameter, and the use of a wider-field optical design.

2. The decision to have the scan mirror rotate 180^{o} from the input beam for viewing of the calibration blackbody. This eliminates errors that might occur (e.g., from polarization effects) with a 90° rotation, at the penalty of increasing the E-W dimension by about 0.1 m.

3. The use of pulse-tube cryocoolers for detector cooling.

The volume (and mass) of the sensor is determined primarily by the large input telescope (see Figure 2 in the Executive Summary). The E-W dimension is determined by the necessary separation of the three telescope mirrors, and by the need for the input beam to clear the secondary mirror while viewing the calibration blackbody. The N-S dimension is dominated by the aperture diameter. The nadir dimension is again largely dictated by the layout of the input telescope, particularly with respect to beam clearances. Some modest reduction might be obtained by rotating the aft optics out-of-plane, but the benefit would be minor; the layout is already quite compact.

The use of cryocoolers to cool the focal planes simplifies the implementation of passive thermal radiators considerably because they can be operated at ~200K to 250K. Substantial radiator area remains necessary to reject the cryocooler compressor heat and to cool the cold optics, though this can be accommodated within the point design envelope.

The presence of the cryocoolers introduces two complications with respect to the mechanical design. The first is the vibration environment caused by the cryocoolers and the need to decouple this vibration from the interferometer (where it would give rise to spurious effects in the interferograms) and from the focal planes. To minimize vibration of the detectors, flexible thermal straps are required to transport the heat from the focal planes to the cryocoolers. The cryocooler vacuum housing (see below) must be connected to the 200K vacuum housing via thermally- and vibrationally-isolating structures (e.g. flexible stainless steel bellows).

The second major issue is the need to house the cold portions of the cryocoolers and the 65K IR assemblies in a common vacuum chamber to permit bench operation of the sensor. Bench operation (at reduced performance) with the 200 K optics at ambient temperature and with the cryocoolers rejecting to ambient temperature is feasible, and so no provisions are made for vacuum housings in these thermal regions.

2.6.1 Optomechanical Concept

The sensor is divided into three temperature regions. The overall housing contains the scan mirror assembly, the input telescope, and the visible optics and detectors, which are maintained at ambient temperature (~300K). An internal and much smaller IR assembly cooled to 200K is thermally isolated from the main assembly, and contains the interferometer and aft optics for the three IR wavebands. A vacuum housing is attached to this 200K assembly, which accepts the three IR beams through windows. Within this vacuum housing, and thermally isolated from it, are three optics assemblies for focusing the IR beams onto their respective detectors. Fiberglas-epoxy (G-10) tubes housing these assemblies provide support for detector focal planes cooled to 65 K through flexible straps connected to the cold head of a redundant pair of pulse-tube cryocoolers. The optomechanical concept is illustrated in Figure 2-20.

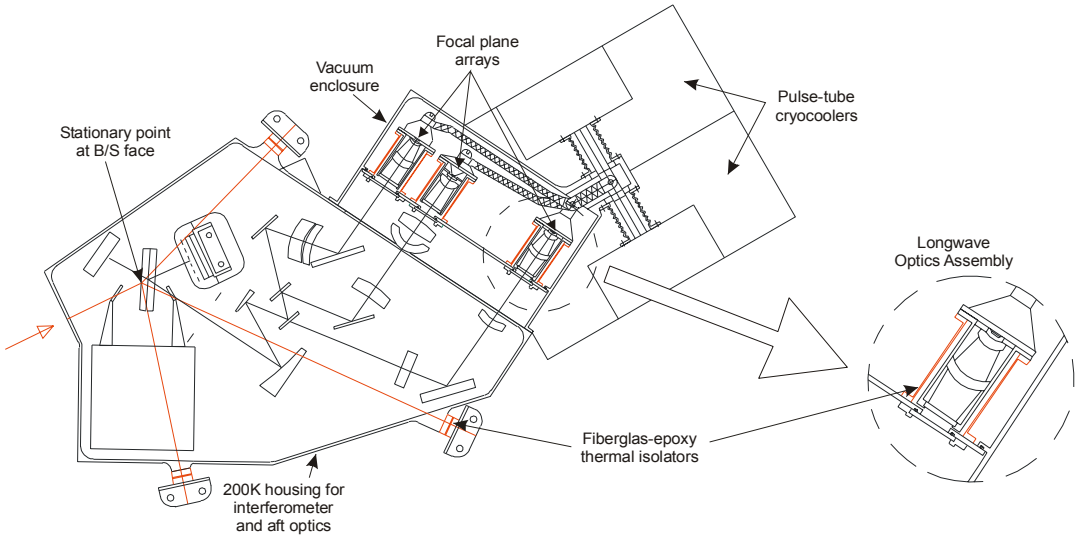

Figure 2-20. The provisions for thermally isolating the ambient (~ 300 K), 200 K, and 65 K modules while maintaining warm-to-cold alignment.

The 300K assembly consists of a rectangular enclosure made up of an aluminum-honeycomb optical bench 84 mm thick with 0.8 mm thick facesheets and four aluminum-honeycomb walls, each 25 mm thick with 0.8 mm facesheets. The optical bench was sized to have a natural frequency of ~150Hz to minimize low frequency interactions. Attached to the input-beam opening is a baffle assembly constructed of 2.5 mm thick aluminum with 10 internal baffle rings, each constructed of 0.8 mm thick aluminum.

The sensor input beam passes through the input baffle to a scan mirror composed of a 51 mm thick silicon carbide (SiC) flat lightweighted by 50%. The scan mirror directs the beam to a three-mirror off-axis telescope. The telescope structure and optical benches are fabricated from aluminum to maintain an athermal design. The primary (largest) mirror is 356 mm in diameter by 65 mm thick and is lightweighted by 50%. The scan mirror uses a two-axis drive assembly mounted to the end wall of the enclosure. This mounting arrangement permits the mirror to be rotated 180^{o} from the input beam (about an axis from the center of the scan mirror to the center of the primary mirror) for viewing of a calibration blackbody. Mounting the scan mirror motor to the optical bench is also feasible, with a slightly more complex mechanism. Pointing errors are likely to be lower in this case. The primary mirror is mounted to the opposite end wall of the enclosure and establishes the nominal E-W length of the sensor. The position of the telescope tertiary increases the E-W length of the sensor by approximately 100 mm.

From the input telescope, the beam reaches a beamsplitter, which reflects visible wavelengths and passes IR wavelengths. Behind the beam splitter is a small ambient-temperature visible assembly with an aluminum honeycomb optical bench 25 mm thick with 0.8 mm thick facesheets. This assembly houses the visible-IR beamsplitter, which is a 94.5%/5.5% visible beamsplitter to direct the beam to daylight and low-light CCD's, with focusing optics subassemblies. A 1.6 mm thick cover for this unit is included in the mass estimate for the sensor. The visible assembly could be assembled and checked out as an individual module. It would be mounted to the main optical bench.

The IR beam from the visible-IR beamsplitter passes into the 200 K assembly. The beam first encounters the Michelson interferometer beamsplitter/compensator. The reflected beam bounces off a commandable mirror that provides a capability for post-launch interferometer alignment. The transmitted beam continues to a displaceable mirror which moves $\pm \sim 5$ mm to generate an interferogram with the necessary spectral resolution plus allowance for turn-around. The output beam from the interferometer passes through beam-splitting optics separating the short-, medium-, and long-wavelength channels. These individual IR beams pass through windows into a vacuum housing, which is maintained at 200 K.

Within the vacuum housing (and thermally isolated from it) are three separate infrared optics assemblies, one each for the short-, medium-, and long-wavelength channels. One of these assemblies is highlighted as an inset in Figure 2-20. Each assembly supports the focusing optics and detector arrays for the respective channel. These assemblies are mounted from fiberglass-epoxy cylinders 50 mm long and 0.5 mm thick, which maintain the focusing optics and detector arrays concentric with each incoming beam. At the same time, the assemblies are thermally isolated from the 200 K vacuum housing so that they can be cooled to 65 K. This construction maintains the warm-to-cold alignment of each IR waveband. Each IR assembly contains a filter, cold stop, and focusing optics mounted in an aluminum housing. A detector array is mounted and aligned to the end of each assembly at the focal plane. Three separate cold straps conduct the heat from the detector assemblies to the cryocoolers. The 65 K long-wavelength detector array has the shortest thermal path to the cryocoolers to minimize the temperature drop to the 60 K cryocooler cold head. The short- and mid-wavelength detector arrays operate at 65 K as well, although operation at 70-75 K would be acceptable for these arrays.

Band-to-band coregistration requires that the detector arrays be precisely located in terms of the IR focal points and elimination of angular clocking between arrays. This issue was not addressed in detail in this study, however the presence of a field stop in the aft optics common to all three wavebands makes modular alignment of the aft optics and detector arrays practical. Detailed design of alignment mechanisms was considered to be beyond the scope of this study.

For high reliability over the ten-year design life of the ABS instrument, two fully redundant pulse-tube coolers are used in the baseline. No thermal switching is incorporated. This is expected to be the most reliable cryocooler configuration [14]. Because one of the cryocoolers is de-energized, the cold straps from the detectors are connected to the midpoint of a copper link between the cold heads of two identical pulse-tube cryocoolers. Thermal isolation of the 250 K cryocooler compressors from the 200 K vacuum assembly is accomplished with a pair of stainless-steel bellows. The details of the 65 K detector arrays, cold straps, and cryocoolers are shown in Figure 2-21.

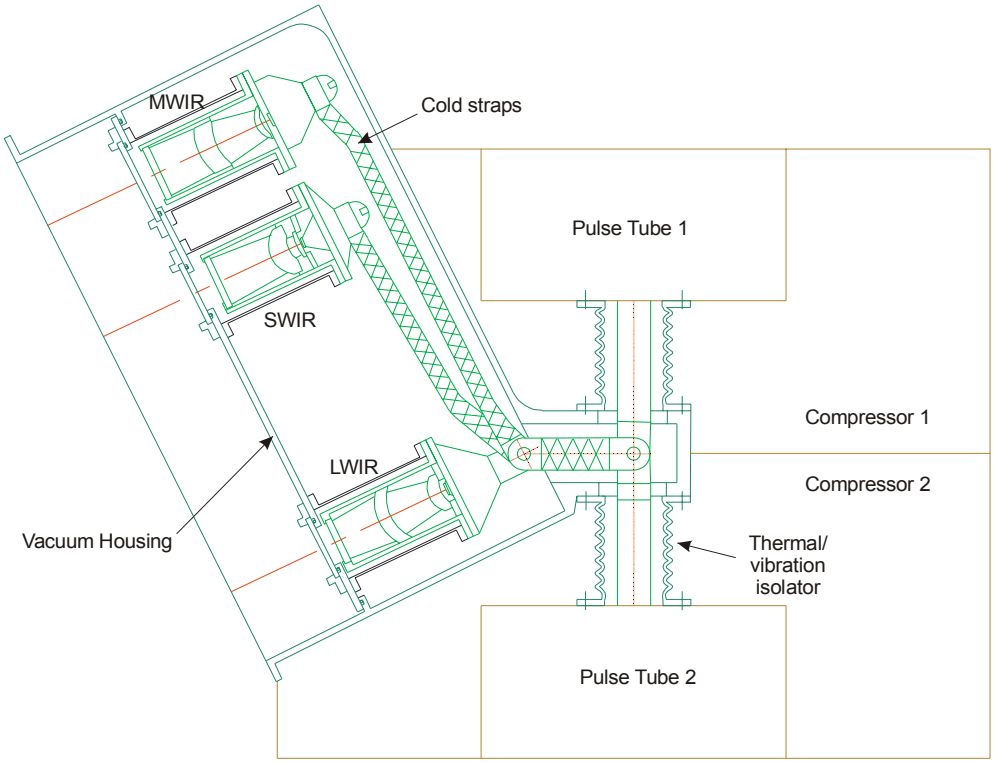

Figure 2-21. The detailed design of the focal planes, cold straps and redundant pulse-tube cryocoolers.

The 65K thermal straps are aluminum foil (99.9% pure) with a thermal conductivity of 231 W/(m K) at ambient temperature. Because of this high purity the thermal conductivity increases as the temperature decreases. At 65 K the thermal conductivity increases to 540 W/(m K) which means that a smaller cross-sectional area is possible, permitting more flexibility in the thermal straps. The thermal conductivity of pure copper is slightly higher than that of pure aluminum at 65 K, but its density is three times higher than aluminum making aluminum the better choice from a weight perspective.

2.6.2 Thermal Design

The ABS point design documented here utilizes a combination of active (refrigerative) and passive (radiative) cooling techniques. The use of large focal plane arrays, which dissipate substantial power, with operation required at 65 K for the LWIR array, makes extension of the 75 K passively-cooled design of Reference 2 impractical. In addition, many flight programs [15] are demonstrating that long-life pulse-tube and Stirling coolers are feasible for deployment in space. A space-qualified pulse-tube cooler has been demonstrated which can be operated at 250 K for increased efficiency. This high-efficiency design [16] is identical to that used as a baseline for the NASA New Millennium Program (NMP) Geostationary Imaging Fourier Transform Spectrometer (GIFTS) mission [17], but it omits the GIFTS two-stage cold head, which is not necessary for this ABS point design because the 200 K cold optics temperature can be readily achieved with a passive radiator.

Radiative coolers are retained to cool the 200 K optics and to operate the cryocoolers at a 250 K heat-reject temperature. Cold operation of the cryocooler compressors improves their efficiency and results in diminished power requirements for the sensor.

Cryocooler Configuration. The cryocooler selected for the ABS point design is a high-efficiency pulse-tube unit, which is illustrated in Figure 2-22. Two such coolers are incorporated in the design, with the cold blocks facing toward each other such that a link can be made between them, and the cold straps to the detectors connected to the midpoint of this link.

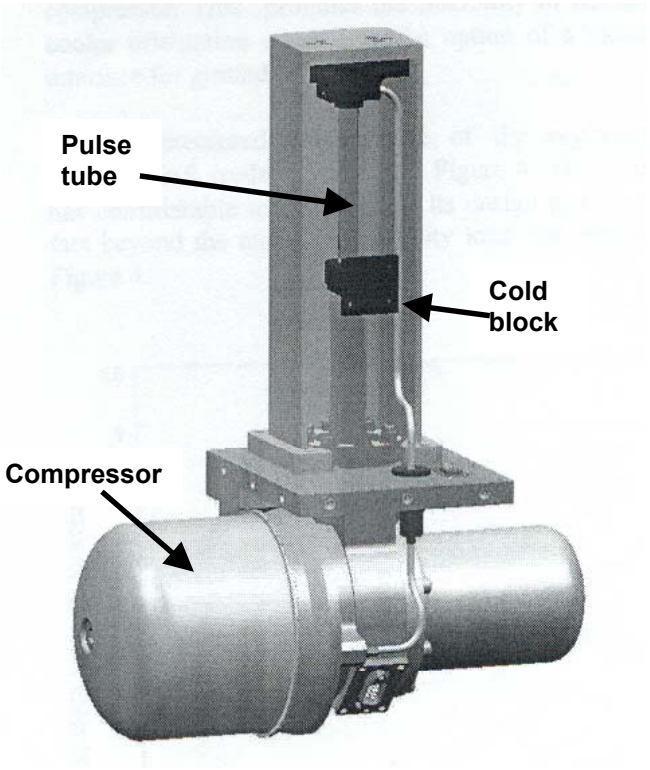

Figure 2-22. The ABS point design cryocooler (one of a redundant pair).

The largest heat load that must be sunk by the operating cryocooler is the parasitic load of the de-energized cooler, which is conservatively estimated to be 800 mW at the 60 K cold-tip temperature. The symmetric arrangement of the cryocoolers and heat straps allows either cooler to bear the 65 K operating heat load. The second-largest heat load is that of the detector focal plane arrays, which dissipate power according to the following general rule [11]:

$$P_{FPA} = N_{pixels}\, P_{preamp} + 3\, C_{load} V^2\, N_{outputs} f_{tap},$$

where P_{FPA} is the power from the FPA, N_{pixels} is the number of pixels in the FPA, P_{preamp} is the power from the pixel preamplifier, C_{load} is the output cable capacitance, V is the signal voltage, $N_{outputs}$ is the number of outputs from the CCD, and f_{tap} is the tap frequency. A conservative 40 μW estimate is made for each pixel preamplifier, and the output cable capacitance is estimated at 500 pF. With a 3 V maximum signal,

and each 48 x 22 array powered and reading out data through the entire interferogram, the estimated power dissipation is 90 mW for the MWIR array, and 140 mW for the SWIR and LWIR arrays. An additional 50 mW is budgeted for the thermal control of each array through joule heating. Parasitic conduction through the G-10 supports and radiation to the 65 K elements is estimated at 160 mW each. Finally, 70 mW is estimated for 100 constantan wires running between the 200 K housing and the 65 K focal planes.

The overall thermal budget for the cryocoolers, including an ample amount of margin to compensate for uncertainties and end-of-life increase in parasitics and/or dissipated heat is shown in Table 2-7. The total 60 K cold-block load of the operating cryocooler is estimated at 2.5 W.

Table 2-7. ABS Cryocooler thermal budget.

Description	Heat	Notes
Dissipated Loads		
SW FPA dissipation	0.20 W	60 mW margin
MW FPA dissipation	0.15 W	60 mW margin
LW FPA dissipation	0.20 W	60 mW margin
FPA control power	0.15 W	Control each FPA to ~ 6 mK [18]
Parasitic Loads		
Redundant cryocooler parasitic	0.80 W	Cold head not optimized for 60 K
65 K conduction load	0.16 W	Fiberglas-epoxy FPA supports
65 K radiation load	0.16 W	Housing, filter, FPA, cold straps
FPA wires	0.07 W	100 constantan wires total
Subtotal	**1.90 W**	
Margin	**0.60 W**	**30%**
Total cryocooler load	**2.5 W**	**60 K cold-tip temperature**

In order to sink a given amount of heat at the cold tip, a much larger amount of compressor power is necessary. The ratio of compressor power consumed to heat removed at the cold tip is referred to as the *specific power*. The best theoretical refrigeration efficiency is that of the Carnot cycle, which has a specific power given by [19]

$$SP_{carnot} = (T_{warm} - T_{cold})/T_{cold}.$$

Here, T_{warm} and T_{cold} refer to the heat-reject and cold-tip temperatures. In practice, demonstrated specific power for pulse-tube and Stirling cryocoolers tend to be about five to ten times higher than that of the Carnot specific power, with the high-efficiency cooler used here representing the lower end of that range. There is also power consumed by the compressor even when no heat is being removed from the cold head, although for our purposes we neglect this since it is hard to obtain accurate figures. In any case there is a substantial amount of margin in the thermal portion of the ABS point design.

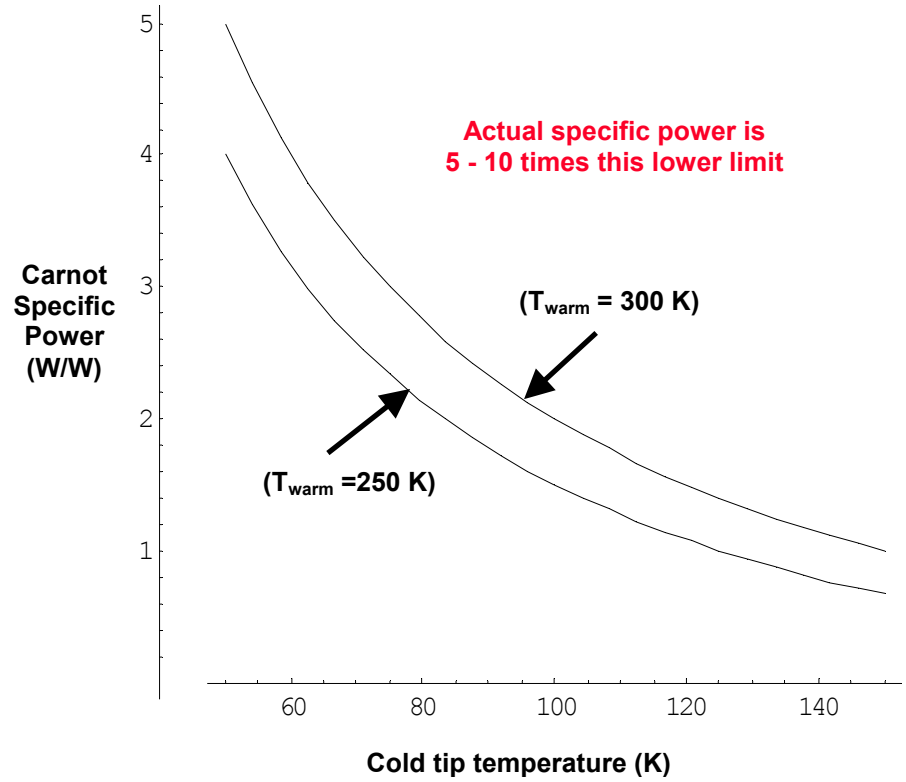

Figure 2-23. The effect on efficiency of rejecting cryocooler heat to a reduced temperature.

Figure 2-23 demonstrates the benefit of rejecting heat to less than ambient temperature: the Carnot efficiency is shown for heat reject temperatures of 250 K and 300 K as a function of cold-tip temperature. Although the savings in power at first appears to be modest, the diminished efficiency of demonstrated coolers means that tens of watts are saved for a 2.5 W heat load at 60 K. The estimated specific power of the ABS point-design cryocooler is ~20 W/W. Since cryocooler waste heat cannot be sunk to the spacecraft bus, a radiative cooler is needed in any case, and operating it at 250 K versus ambient temperature is relatively straightforward.

Although a potentially greater benefit would be obtained by optimizing the cold head to reduce the 800 mW parasitic heat when used in a redundant configuration, it was decided to use only the demonstrated performance of the cooler. Optimizing the cold head would likely be worthwhile for a flight instrument, however.

Radiative Cooler Design. There are three passive thermal radiators (see Figure 1 and Figure 2-24) to maintain the ambient (~ 300 K), 250 K, and 200 K sensor components at their nominal temperatures. The first radiator, the smallest of the three radiators, operates at ambient temperature, and radiates heat from the moving-mirror assembly, the two-axis drive for the scan mirror, metrology electronics, and other miscellaneous components located within the sensor. The second radiator operates at approximately 250K to radiate heat from the calibration blackbody (maintained at 290 K) and to efficiently operate the cryocooler compressors. Because of the large heat input from the cryocooler compressors, this is by far the largest of the three radiators. The third radiator (supported from the 250K radiator to minimize heat input) will cool the 200K IR optics assembly. The 200 K radiator is sized assuming an uncontrolled temperature of 180 K. It controls the cold optics assembly at the 200 K set point. Three main heat sources comprise ~99% of the total 200 K radiator heat load. These sources are the thermal radiation from the 300 K surroundings to the 200K housing and thermal strap, the thermal inputs through the holes in the housing (for IR beams and the moving mirror mechanism), and the thermal radiation from the solar array (~30% of the total) to the radiator. The 200 K radiator will be located approximately 0.2 m to 0.25 m from the 200 K assembly; therefore a thermal strap will connect them. The 20K margin is presumed to be adequate for the temperature drop along this thermal strap, and for the incorporation of some (unspecified) amount of joule heating for temperature control.

For the purposes of radiator sizing, a hemispherical view of cold space is assumed. This requires a seasonal reorientation of the spacecraft (e.g. a "yaw flip") at the equinoxes to prevent sunlight from illuminating the radiator surfaces. Because solar arrays may be present on both the illuminated and shadowed sides of the spacecraft, it is assumed that a solar array 1m wide by 4m long is located above the thermal radiators, beginning at a distance of 1m. This warm solar array will radiate heat to the cooler radiators on the sensor. Sun glint from the array is not accounted for. Radiator sizing assumes solar absorptivity and IR emissivity of $\alpha = 0.17$ and $\varepsilon = 0.78$ respectively at EOL, e.g. assuming the use of a silver-backed glass radiator (such as an Optical Surface Reflector (OSR)). The radiator stages are nested to form a three-stage radiative cooler similar in principle to that of Reference 2, minimizing parasitic heat coupling between stages.

In the event that the "yaw flip" maneuver is not performed seasonally by the spacecraft, there will be direct solar input to the radiators. With the radiators inclined 23.5 degrees to the ecliptic at solstice, the solar input alone will exceed the capacity of the 200 K radiator at EOL. Therefore, a sunshade will be required for this radiator if there is no “yaw-flip” maneuver. In the case of the 250 K radiator, whose temperature serves mainly to decrease the cryocooler power, an appropriate course of action would simply be to allow its temperature to increase to near ambient and accept the penalty in terms of reduced cryocooler efficiency. With a heat load increased to ~165 W at solstice, this radiator would warm to about ~280 K with a ~30 W increase in sensor consumption due to the increase in specific power for the cryocooler. The ambient-temperature radiator would require only a modest amount of growth (0.14 m^2 to 0.18 m^2), which can be accommodated within the sensor outline.

The thermal budget for the radiative coolers is summarized in Table 2-8. The sizing and layout of the coolers is shown in Figure 2-24.

Table 2-8. Thermal budget for passive radiative coolers.

Description	Heat	Notes
Ambient radiator: 49 W @ 300 K, Area = 0.14 m^2		
Interferometer moving mirror	8 W	Mechanism dissipation
Scan mirror motor	20 W	
Metrology source	4 W	Laser dissipation
Sensor electronics	7.5 W	IR preamplifiers
Radiation from solar array	1 W	1 x 4 m, 1 m from radiator
Conduction from spacecraft	5 W	
Margin	3.5 W	8%
250 K radiator: 105 W @ 250 K, Area = 0.61 m^2		
Cryocooler compressor heat	50 W	2.5 W load, 20 W/W sp. power
Cryocooler EOL margin	20 W	40% EOL growth allowance
Calibration blackbody	7 W	Controlled at 290 K
Radiation from solar array	8 W	0.0467 view factor
Margin	20 W	24%
200 K radiator: 10.2 W @ 180 K, Area = 0.22 m^2		
Radiation from 300 K to housing	4.60 W	IR ass'y and vacuum housing
Radiation thru housing apertures	2.38 W	Moving mirror and IR beams
Conduction thru housing supports	0.15 W	G-10 flexures to 300 K
Conduction thru SS bellows	0.23 W	Vibrational isolators to 250 K
Radiation input from Earth	0.07 W	Emission and solar reflection
Radiation input from solar array	3.07 W	0.0396 view factor
Heat loss to 65 K	(-0.32.W)	

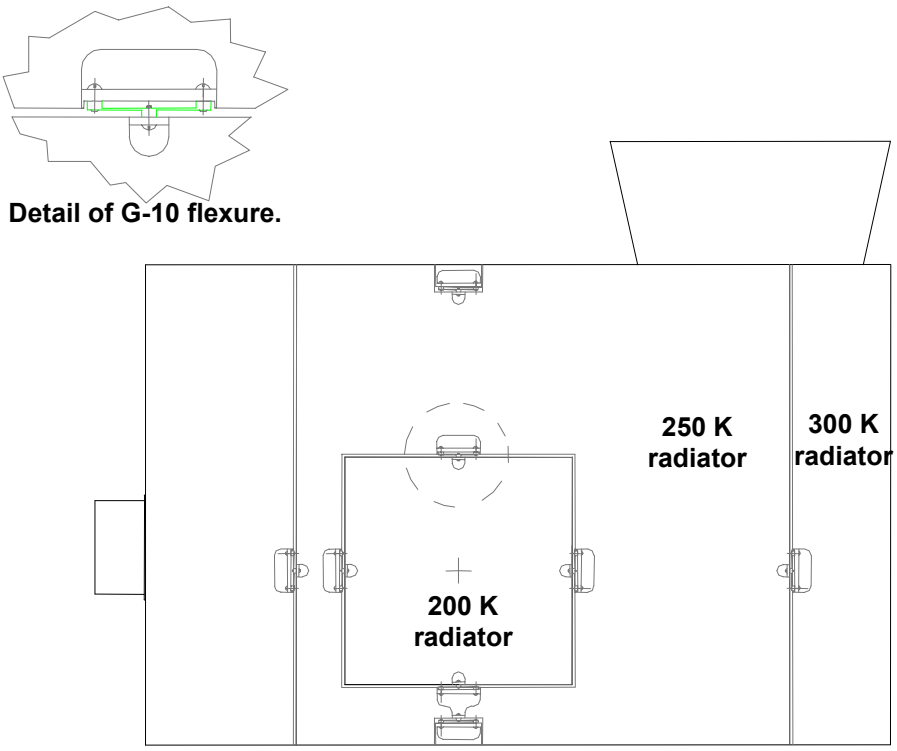

Figure 2-24. The layout and sizes of the ABS radiative coolers.

2.6.3 Sensor Mass Estimate

In Table 2-9, the detailed mechanical design presented in this section is used to estimate the ABS point design sensor mass. The system mass, which includes electronics modules and cabling external to the ABS sensor is presented in Section 2.9.

Table 2-9. ABS Sensor mass estimate.

Description	Mass (kg)
Input aperture cover	5.5
Radiator cover	2.5
Optical bench (3" Al. honeycomb)	11.0
Ambient optics assemblies	13.9
200 K optics assembly	11.2
65 K optics assembly	1.5
Blackbody calibration source	1.2
Scan mirror (SiC, 50% lightweighted)	10.2
Scan motor assembly	3.0
Baffles, internal and external	9.1
Housing (1" Al. honeycomb)	16.6
Moving mirror assembly	1.8
Radiation shielding	0.1
Magnetic shielding	0.9
Cryocoolers (2)	8.0
Passive thermal radiators	8.6
Sensor estimate	**105.1**
Margin (20%)	**21.0**
ABS Sensor mass estimate	**~126**

2.7 Electronics System

The architecture of the ABS electronics is largely unchanged from the original design work of Reference 2. This architecture is illustrated in Figure 2-25. The assumed implementation of the ABS electronics draws heavily on the MIT/LL brassboard test program [20] for the GOES High-resolution Interferometer Sounder (GHIS). In general, the sensor data flow follows a path from very high unprocessed rates to a final output rate of ~ 9.9 Mbps, which meets the January 2001 TRD maximum of 10 Mbps, although with zero margin. The electronics system also coordinates automatic system operation, execution of ground-commandable functions, and collection of housekeeping telemetry data.

With the exception of the metrology laser and the fast 16-bit A/D converters used in the longwave IR band, all components are available in space-qualified versions. The metrology laser and 16-bit A/D converter are identified as technological risk items as noted in Section 2.11.

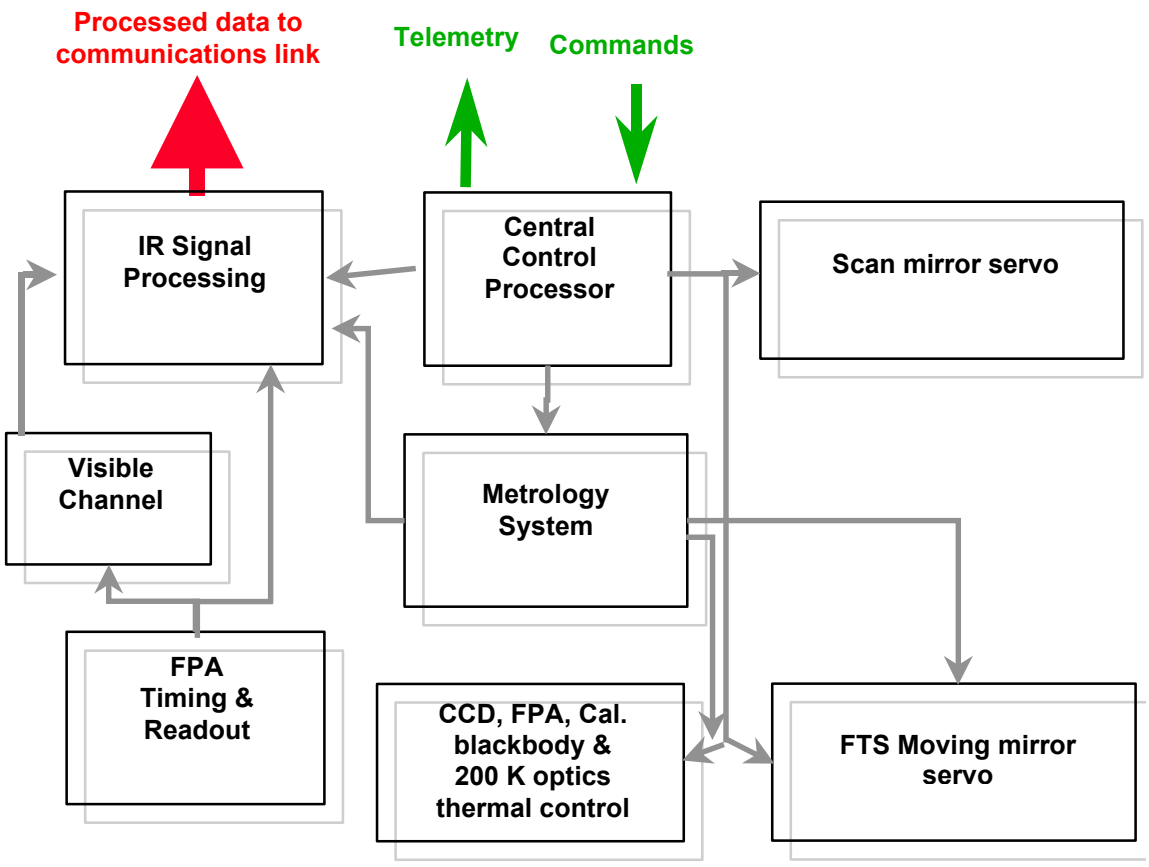

Figure 2-25. ABS electronics system architecture.

2.7.1 Instrument Control Electronics

Implementation of controllers is the same as in Reference 2, as summarized in Table 2-10. The reader is directed to this earlier ABS work for implementation details. The only differences are the use of a larger scan mirror drive amplifier for the 30 cm aperture, the use of two CCD's, and thermal control of the blackbody calibration source and cold optics as well as the IR FPA's.

Table 2-10. ABS Controller implementation (see Ref. 2)

Description	Power	Mass	Notes
Instrument control processor	0.2 A @ +5 V	0.5 kg (one 6" x 8" board)	8-bit microprocessor & memory
FPA timing logic	0.3 A @ +5 V	0.5 kg	ASIC
FPA readout drive signals	0.2 A @ +15 V 0.2 A @ -15 V	0.5 kg	Analog electronics
Scan mirror servo	0.2 A @ +5 V 0.05 A @ ±15 V	0.5 kg	Sensor, A/D & DSP
Scan mirror motor drive	0.67 A @ ±15 V	0.5 kg	20 W Power amplifier
FTS moving mirror servo	0.3 A @ +5 V 0.15 A @ ±15 V	1.0 kg (two 6" x 8" boards)	Metrology, A/D & DSP
FTS moving mirror drive	0.27 A @ ±15 V	0.5 kg	8 W Power amplifier
Visible CCD thermal controllers	0.8 A @ +5 V 0.03 A @ ±15 V	1.0 kg (two 6" x 8" boards)	Thermoelectric stabilization of two CCD's
Cryocooler/FPA thermal controller	0.8 A @ +5 V 0.015 A @ ±15 V	0.5 kg	Joule-heating of FPA's to a common setpoint
Calibration blackbody thermal controller	0.8 A @ +5 V 0.015 A @ ±15 V	0.5 kg	Joule-heating of blackbody to its setpoint
200 K radiator thermal controller	0.8 A @ +5 V 0.015 A @ ±15 V	0.5 kg	Joule-heating of 200 K radiator to stabilize cold optics temperature.

2.7.2 FPA Sampling Metrology Electronics

The metrology system both provides feedback acts for the FTS moving mirror servo controller and generates sampling triggers for the IR channel FPA's. A thorough description of its operation is given in Section 3.5.2 of Reference 2. The principle employed here is the same. The sampling interval for the IR is initiated with zero crossings of the I signal, as shown on the right side of Figure 2-26. When the zero crossing is detected, a clock edge is produced by the field programmable gate array (FPGA). The FPGA generates the timing pulses for the FPA. The clock edge triggers the beginning of the FPA integration. After a fixed time interval for sampling, the edge of a second clock is produced by the FPGA and the single integration stops. The diagram shows a single integration period for one fringe of the metrology system; band 2 is the only band that will utilize every fringe and thus every other zero crossing signal. Bands 1 and 3 will use every zero crossing signal in determining the sample time. Multiple samples are collected from each pixel and are held in a counter until the required number of samples for decimation is obtained. The single decimated sample is then recorded, having reduced noise compared to a single IR sample.

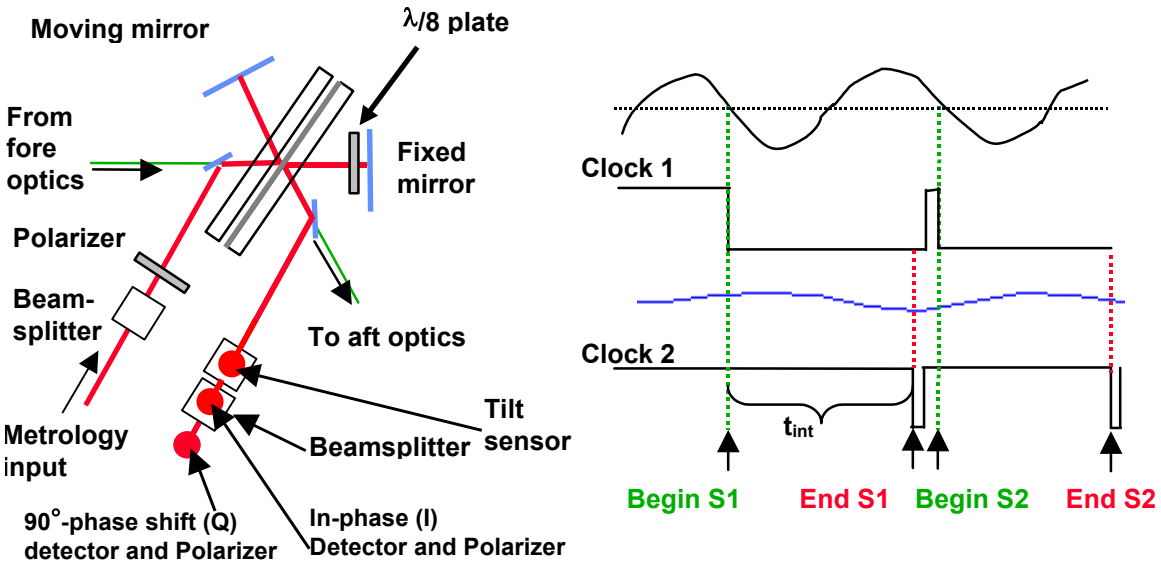

Figure 2-26. The arrangement of the metrology optics, along with the MWIR FPA sampling. The SWIR and the LWIR sample twice within this sampling period.

The tilt error may be characterized, and more refined corrections of second-order velocity errors made, by injecting an unpolarized metrology beam along with the polarized beams used for interferogram sampling and decimation. Imaging this unpolarized beam onto an InGaAs detector produces metrology fringes which may be used to characterize the moving mirror tilt through its stroke.

A laser of 1.55 μm would provide appropriate sampling for this interferometer system. This wavelength was chosen to take advantage of the availability of commercial communications lasers in the 1.5 μm diode family. This is an InGaAsP laser where the doping is varied to tune the laser near 1.5 μm. Using a currently available commercial InGaAs FPA and a 5 mW laser, a signal to noise of about 200 would be required to measure a 7-μrad tilt. For a higher power laser emission of 100 mW, which may prove challenging to obtain for this wavelength, a signal to noise level of about 600 is anticipated to achieve a 4-μrad tilt precision. Even if the power is sufficient in commercial lasers of this wavelength, they normally do not support the lifetime and spectral stability that would be required for this metrology system. Commercial lasers can be modified to provide the required performance, as was done by NASA Goddard for the GHIS program [20]. Currently other programs/missions will be developing long lifetime lasers for their needs, so ABS will utilize those development efforts.

2.7.3 IR Signal Processing Electronics

As was the case with the earlier ABS point design of Reference 2, the assumed IR signal-processing architecture uses a decimating finite impulse-response (FIR) digital filter algorithm [21] in the place of on-board FFT spectral conversion. The implementation of this scheme is done in parallel on the MWIR and LWIR channels in order to keep readout rates of individual FPA output taps low as described in Section 2.5.1. The signal flow for the LWIR processing chains is shown in Figure 2-27. Similar diagrams would apply for the MWIR and SWIR channels except for frame rates and digitization.

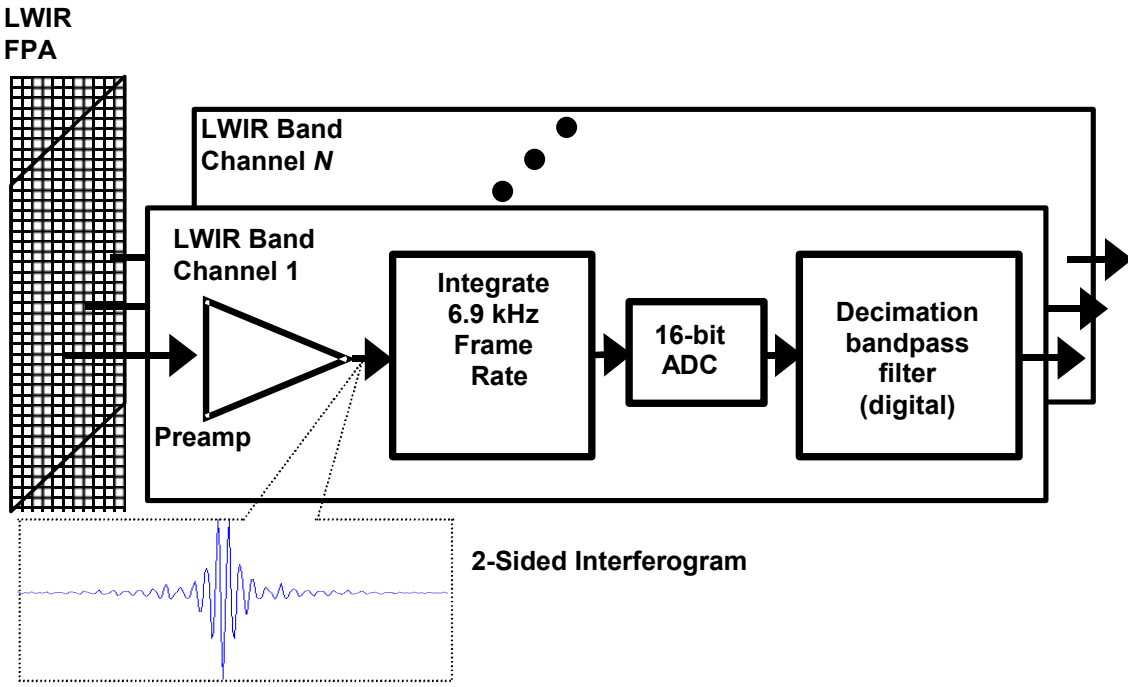

Figure 2-27. The signal processing flow for the LWIR channels.

Implementation of the decimating FIR filters for the three bands is illustrated in Table 2-11. All three wavebands utilize complex FIR bandpass filters designed for 3 dB passband ripple and -60 dB aliasing attenuation.

Table 2-11. IR Signal processing summary.

Parameter	SWIR band	MWIR band	LWIR band
Samples per fringe	2	1	2
Oversampling factor	23	12	23
Digitization	12 bits	16 bits	16 bits
Decimation factor	20	10	20
Number of filter taps	292	98	296
Storage required (Kbytes)	584	294	708
Access rate (Mbytes/s)	220	76	180
Memory required (chips)	2	1	2
Required access time (ns)	36.4	52.6	44.4
Memory power (W)	4.4	1.5	3.6
Multiply rate (Mops/s)	102.9	34.5	83.1
FPGA's required (chips)	5	2	4
FPGA power (W)	3.1	1.0	2.5
Number of cards	2	2 (4 chains each)	4 (4 chains each)
Total Power (W)	7.5	2.6	6.1

The performance of the decimating FIR filters is shown in Figure 2-28.

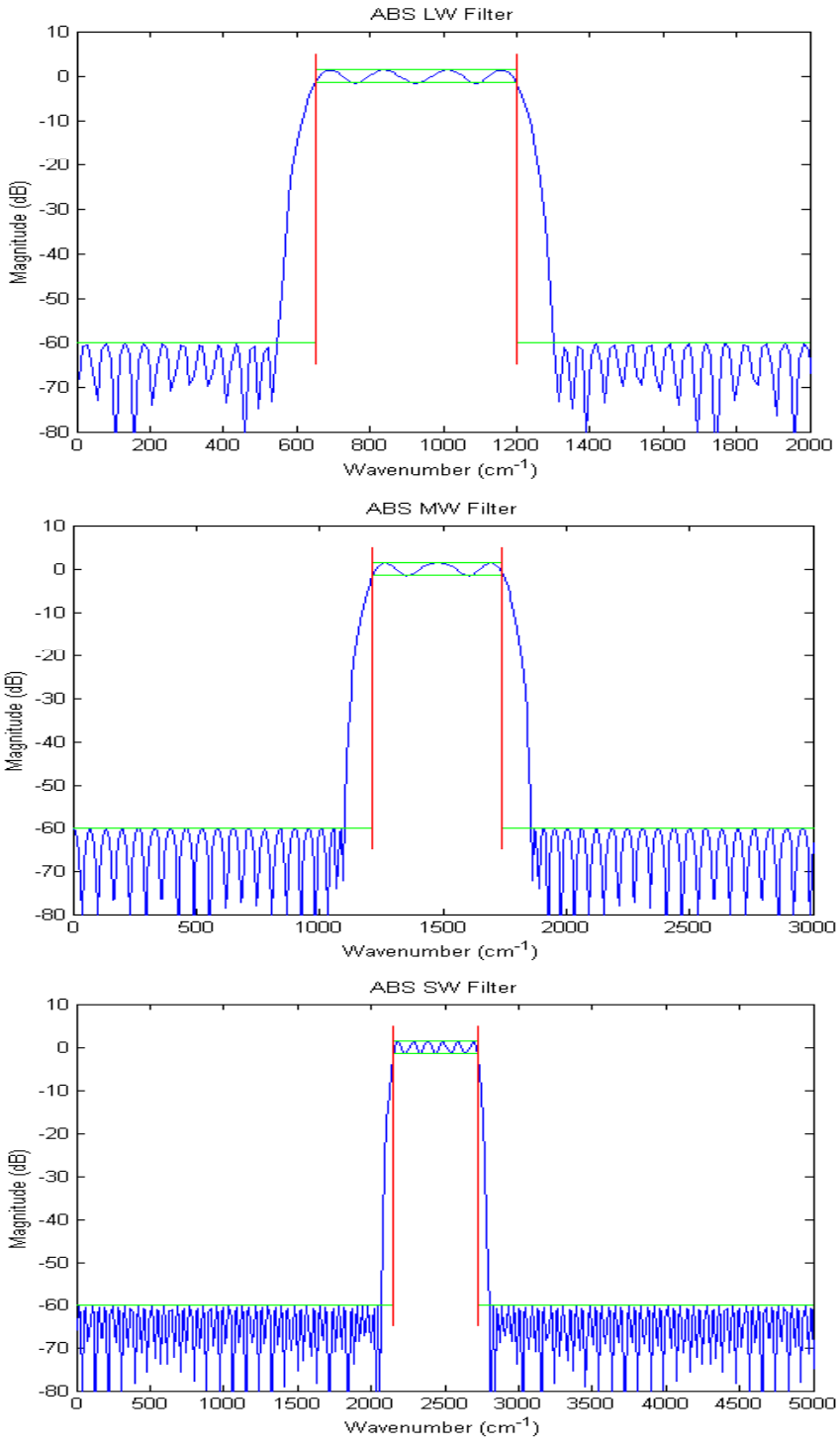

Figure 2-28. Performance of the decimating FIR filters for the three IR bands.

The use of 16-bit A/D's in the LWIR and MWIR channels results from the stringent NEdN requirements of the January 2001 TRD. In order to meet these requirements it is necessary to reduce the quantization noise of the LWIR and MWIR detectors well below the detector noise. The effect on the overall system noise is shown in Figure 2-29, where the modeled NEdN is illustrated for 14-bit and 16-bit quantization.

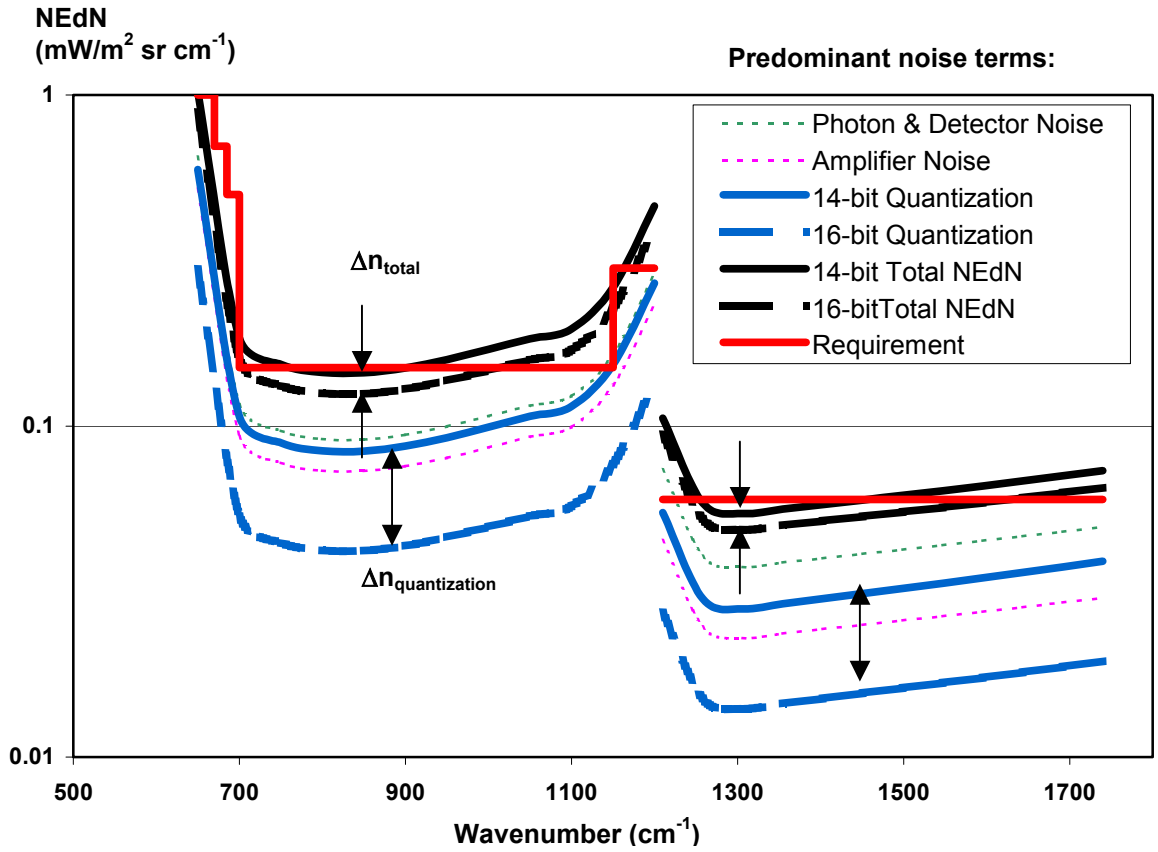

Figure 2-29. The rationale for using 16-bit A/D converters.

Implementation of these multiple signal processing chains is summarized in Table 2-12.

Table 2-12. ABS Signal processing implementation (see Ref. 2)

Description	Power	Mass	Notes
Visible signal processing	0.05 A @ +5 V 0.01 A @ ±15 V	0.5 kg (1 board)	Preamp and 14-bit A/D converter
SWIR signal processing	0.1 A @ +5 V 0.01 A @ ±15 V	0.5 kg	Preamp, 12-bit A/D converter
SWIR decimating FIR digital filter	1.5 A @ +5 V	1.0 kg (2 boards)	Memory & FPGA's
MWIR signal processing (one of 8 chains)	0.1 A @ +5 V 0.01 A @ ±15 V	0.5 kg	Preamp, 16-bit A/D converter
MWIR decimating FIR digital filter	0.52 A @ +5 V	1.0 kg (2 boards, 4 chains each)	Memory & FPGA's
LWIR signal processing (one of 16 chains)	0.1 A @ +5 V 0.01 A @ ±15 V	0.5 kg	Preamp, 16-bit A/D converter
LWIR decimating FIR digital filter	1.22 A @ +5 V	2.0 kg (4 boards, 4 chains each)	Memory & FPGA's

2.7.4 Electronics System Power Consumption

The estimated consumption of conditioned power given in Table 2-10 and Table 2-12 for the control and signal processing electronics are used in Table 2-13 to derive the overall electronics system power consumption. The ABS sensor and system power consumption are estimated, in the context of spacecraft accomodation, in Section 2.9.

Table 2-13. Electronics system power consumption.

Description	+5 V cond. (A)	±15 V cond. (A)	Power (W)
Instrument control processor	0.2		1.0
FPA timing logic	0.3		1.5
FPA drive signals		0.4	12.0
VIS signal processing	0.05	0.01	0.6
SWIR preamps and ADC's	0.1	0.01	0.8
SWIR decimating FIR digital filter	1.5		7.5
MWIR preamps and ADC's	0.8	0.08	6.4
MWIR decimating FIR digital filter	0.52		2.6
LWIR preamps and ADC's	1.6	0.16	12.8
LWIR decimating FIR digital filter	1.22		6.1
Scan mirror motor		0.67	20
Scan mirror servo	0.2	0.05	2.5
FTS moving mirror motor		0.27	8
FTS moving mirror servo	0.3	0.15	6
VIS CCD thermal controllers	0.8	0.03	5.0
IR FPA thermal controller	0.8	0.15	4.5

Description	+5 V cond. (A)	±15 V cond. (A)	Power (W)
200 K thermal controller	0.8	0.15	4.5
Blackbody thermal controller	0.8	0.15	4.5
Conditioned power supply (A)	10 (50 W)	1.88 (57 W)	107
Power supply consumption @ 75% efficiency (W)	17	19	36

2.7.5 ABS Instrument Data Rate

Table 2-14 summarizes the ABS point design data rate, and the factors that drive it. The number of samples in the LWIR, MWIR, and SWIR listed in the Table reflects the total number of spectral samples in the spectral range with allowance for achievable decimation factors. The resulting data rate is 11.35 Mbps before buffering. In order to accommodate the data in a 10 Mbps downlink as specified by the January 2001 TRD, the data must be buffered. The data collection time (i.e., step time and slew time) so by itself is not long enough to simply collect data and transmit the data during the next step, settle and data collect period. By buffering 100-87.5% = 12.5% of the interferogram data for four rows, containing a maximum of 168 steps, the data can be downlinked at 9.9 Mbps provided 715 Mbits of storage is available. By buffering data during the entire hour, the data rate can be minimized to 9.3 Mbps.

Table 2-14. ABS point design data rate.

	Bits/Pixel	Number of Pixels	Number of Samples	Frame Rate	Product of real and imaginary factor and bit trimming factor	Data bits/sec (Mbps)	Data bits per stare (Mb)		
LWIR	18	1056	1034	0.333	1	6.55	19.65		
MWIR	18	1056	517.28	0.333	1	3.28	9.83		
SWIR	14	1056	257.64	0.333	1	1.27	3.81		
Visible	14	105600	1	0.333	0.5	0.25	0.74		
						Total Earth Data bits/sec (Mbps	**Total Data (Mb)**	**Total data (Mb) for all integrations alone**	
						11.34	34.03	28589.3	
	Cals/Hour	**Hot cals (F+B)**	**Cold cals (F+B)**	**Frame Rate**	**Data bits/interferograms (Mb)**		**Cal data bits per cal stop (Mb)**	**Total cal data bits for all cal stops (Mb)**	
Calib.	6	12	12	.0333	34.03		816.84	4901.02	
								33490.32	**Total data in 1 hour (Mb)**
								9.9	**Data Rate Buffered (Mb)**
								9.3	**Smallest data rate in 1 hour**

2.8 Point Design Performance Estimate

The need to *simultaneously* meet the requirements of Section 1 necessarily required a validation process as the point design took shape. Although many of the trade studies of Reference 2 were not re-examined in this work, the design process remained iterative in nature. This iterative process made it necessary to model the radiometric performance of the evolving point design in order to verify that NEdN requirements were met. At the same time, simulations of retrieved water vapor and temperature profiles were used to verify that the modeled NEdN (which differs in form from the flat-band January 2001 TRD curves) could produce atmospheric soundings in accordance with the needs of the end-users. The design formulation and validation process is illustrated graphically in Figure 2-30.

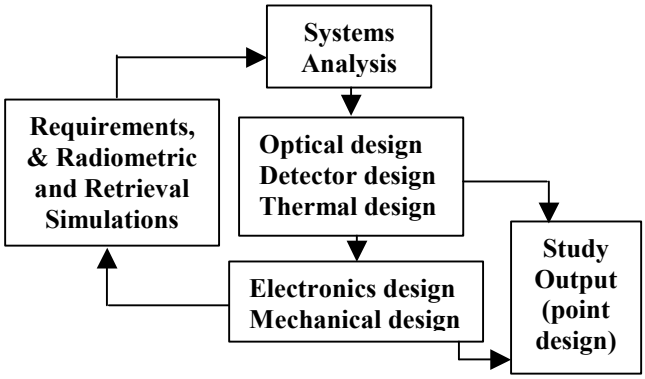

Figure 2-30. The ABS point design formulation/validation process.

2.8.1 Radiometric Modeling

The radiometric model used for ABS point design performance validation is discussed in detail in Reference 2, and its validation against an aircraft interferometer sounder is discussed in Reference 13. The model uses the optical and thermal configuration of the instrument as tabulated in Section 2.5.2 to determine the scene and background flux. It considers the effect of several noise sources within the instrument as illustrated in Figure 2-31 and generates predictions of NEdN across the three instrument wavebands. The modeled NEdN for the ABS point design described in this report is shown in Figure 2-32.

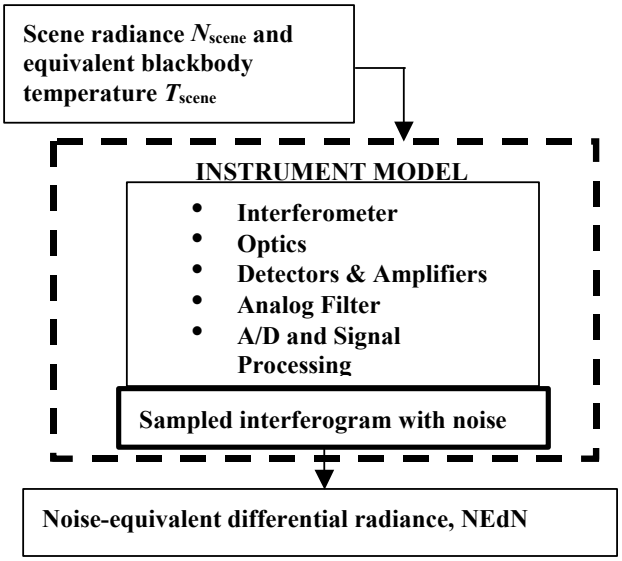

Figure 2-31. FTS radiometric and noise model.

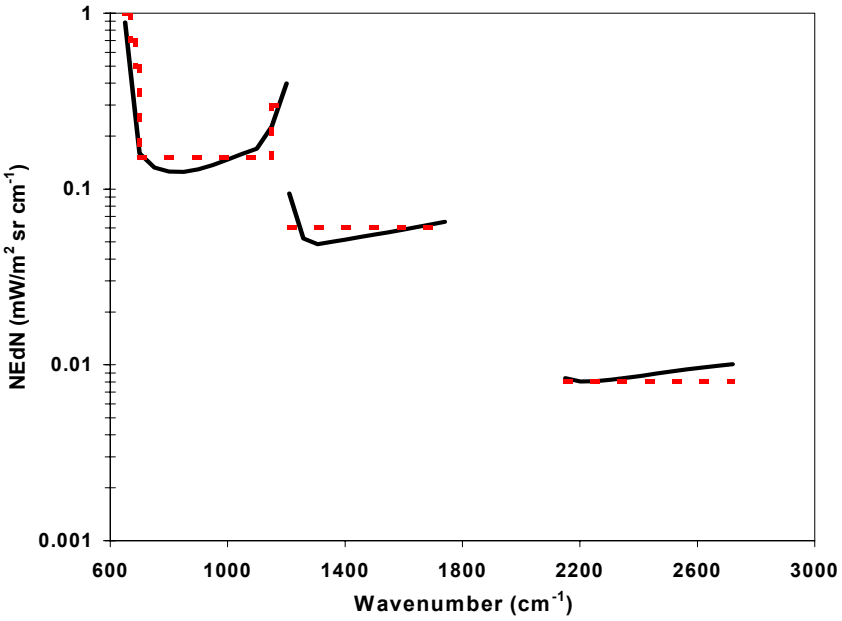

Figure 2-32. Modeled NEdN of the ABS point design.

An important consideration in the radiometric modeling of the design is that detector array statistics are not incorporated in the model. Although historically not an issue, it is important here because IR detector arrays have random distributions of parameters such as responsivity and detector noise that give rise to substantial variations over the array. Figure 2-32 is meant to be representative of the median NEdN of an instrument such as the ABS point design that employs large IR detector arrays. The detector variations illustrated in Figure 2-19 are expected to be representative of variations in NEdN that may be expected from an instrument.

2.8.2 Retrieval Performance Model

The NESDIS January 2001 TRD requirements of Section 1 are chosen largely based on testability. Table 1-1 was included to illustrate the top-level user requirements, against which the January 2001 TRD was validated. Past efforts at MIT/LL in the area of high-spectral-resolution atmospheric sounders have led to the development [22] of a retrieval performance model for such sensors. This model allows the RMS error of retrieved temperature and humidity profiles to be estimated as a means of validating sensor performance. The structure of the model is illustrated in Figure 2-33.

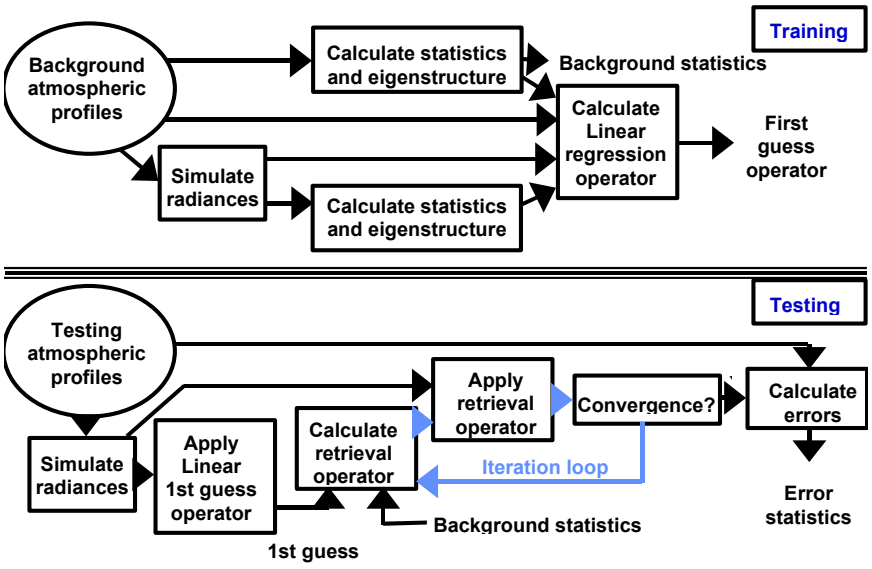

Figure 2-33. Sounder retrieval performance model.

The retrievals were performed by a solution of the radiative transfer equation through an iterative technique. The RMS temperature error versus pressure was computed using profiles from the NOAA88b data set described by the weather products test bed document from NOAA [23]. This data set was used as part of a benchmarking comparison against the retrievals performed at the Cooperative Institute for Meteorological Satellite Studies (CIMSS) at the University of Wisconsin. After limiting the data set to within +/- 65 degrees latitude, a 10 to 1 ratio was used to form the testing set from the training set, yielding 596 profiles for testing. The profiles were chosen to be an exact match to the profiles used at CIMMS for their retrievals. The channel coverage extended between 650 and 2450 cm^{-1}, with every spectral channel used for the linear regression first guess and 239 selected channels used for the physical retrieval. Note that the retrievals were performed using longwave channels that extend to 650 cm^{-1}. Although this wavenumber is beyond the 664-cm^{-1} detector cutoff, some wavelength coverage exists at longer wavelengths as the detector falls to zero responsivity. When responsivity of the detector becomes very low and the retrieved information becomes noisy, the retrieval process reduces the weighting of the noisiest channels. The retrieval channel set represents an improvement over that of the first ABS study but it was not fully optimized for this study. Using the UW-CIMSS channel set did not improve the performance results.

The retrieved temperature results with 0.5 km resolution were layer-averaged to the upper limit of the NWS specification of 0.5 km in the surface to 500-hPa region, 2.0 km in the 300- to 500-hPa region, 2.0 km in the 300- to 100-hPa region, and 3.0 km in the region from 100 hPa upwards. The retrieved water vapor results, in the units of relative humidity, were layer-averaged to the upper limit of the NWS specification of 0.5 km in the surface to 500-hPa region, 2.0 km in the 300- to 500-hPa region, and 2.0 km in the 300-to 100-hPa region. The modeled retrieval performance of the ABS point design described in this report is shown in Figure 2-34 along with curves generated from the ABS TRD NEDN values. In order to include the effects of forward model error, we have included a constant 0.2 K error term which is included in the computation of the rms error.

The benchmarking with CIMSS has led to temperature and water vapor curves that describes the differences between the Lincoln Laboratory retrievals and the CIMSS/UW retrievals in the retrieval algorithm, the channel set coverage in the physical retrieval, coverage of surface emission, and any unstated other operational assumptions. The curves in Figure 2-35 show rms temperature error differences of about 20% and rms relative humidity error differences from ~20% near the surface to ~70% higher up. This indicates general temperature agreement at altitudes above ~ 700 hPa and general water vapor agreement at altitudes below ~500 hPa. However, the Lincoln retrievals do not meet the specification of 10% RMS relative humidity error below 600 mb. Applying the benchmarking curves to the retrievals in the previous figure implies that the RMS temperture error and RMS relative humidity error specifications can be met until below 900 hPa by UW retrievals using the NEDN values from this ABS Point Design. Improvement in performance of the LL retrievals below 700 hPa may require either an explicit treatment of surface emission or an improvement to the physical retrieval model iteration through weighting the input from the linear regression first guess, as suggested by Jun Li of CIMMS/UW.

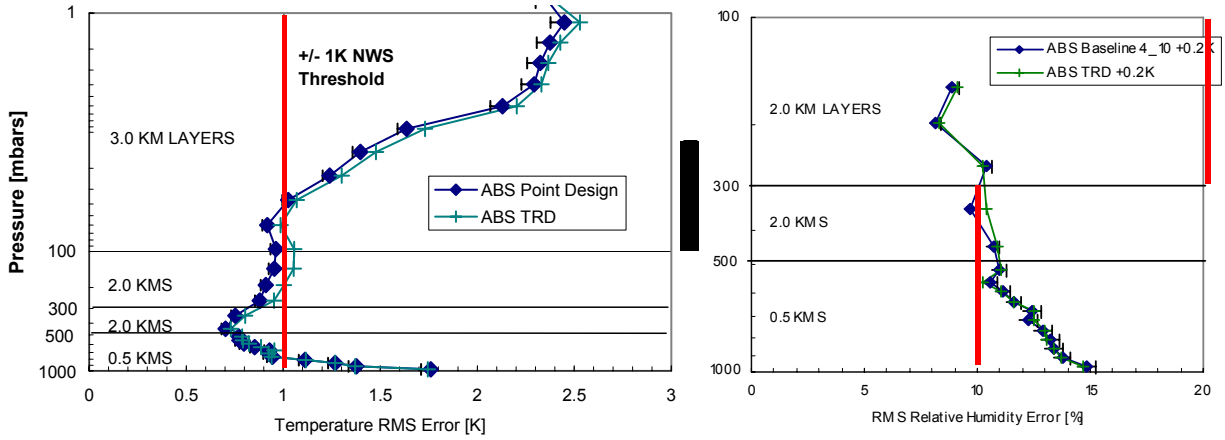

Figure 2-34. Modeled retrieval error of the ABS point design.

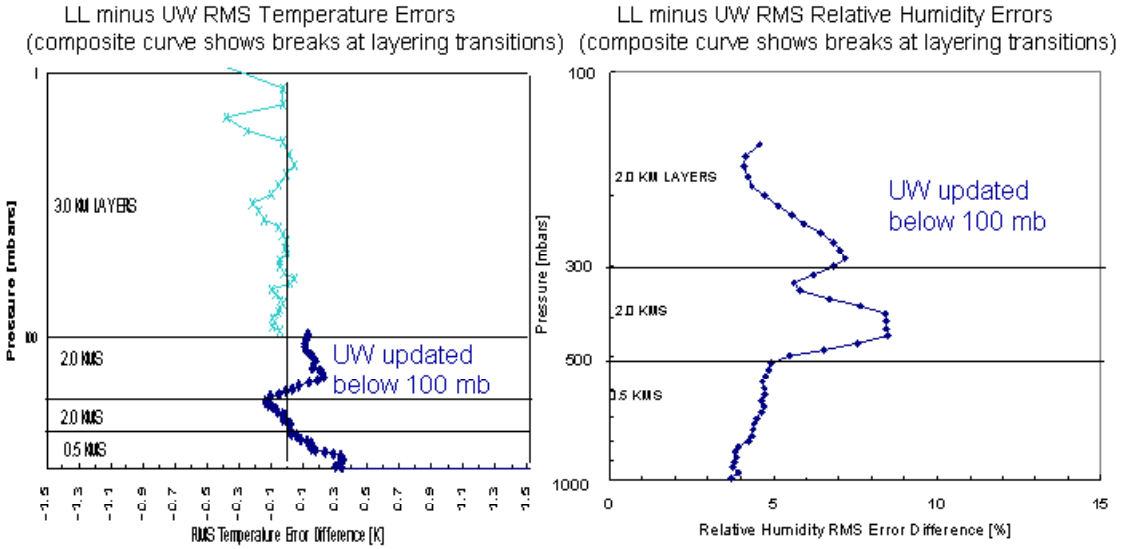

Figure 2-35. Benchmarking curves from temperature and water vapor comparisons.

2.9 Spacecraft Accommodation Issues

At the time of the original ABS design study documented in Reference 2, one of the requirements was that the instrument point design should be compatible with spaceflight on the GOES-N spacecraft. During formulation of the NESDIS January 2001 TRD that constraint was removed, although spacecraft interface goals were defined in that document (see Section 1.4).

The ABS point design volume is approximately 1.7 m (E-W) by 1.25 m (nadir-anti nadir) by 0.7 m (N-S) as illustrated in Figure 2 of the Executive Summary. This is substantially larger than the current sounder. As has been commented on elsewhere in this document, this volume is dictated largely by the optical layout which itself was dictated by the optical field implicit in the coverage rate and NEdN requirements. For this reason, the January 2001 TRD spacecraft accommodation "goal" is not met.

As a means of illustrating the reason the ABS point design volume has increased over the designs of References 2 and 3, consider Figure 2-36. This illustrates three optical designs that were formulated in the course of this work. The first had a 160 x 480 km field, and was nearly sufficient to meet NEdN and coverage requirements in the absence of "overhead" allowances for image rotation, calibration and star sensing as discussed in Section 2.2. This system fits within a one cubic meter volume. The NEdN is a factor of 1.4 larger than the January 2001 TRD [24] at 700 cm^{-1}. For reference, it is a factor of 1.3 larger at 700cm^{-1} than the LL ABS point design. This value accommodates a 14-bit ADC for risk reduction. The performance of this design in the realm of the retrievals is very comparable to the ABS January 2001 TRD performance curve shown in Figure 2-34. Forcing the NEDN to meet the January 2001 TRD requirement at the expense of coverage implies only 68% coverage of the 62 degrees local zenith angle area.

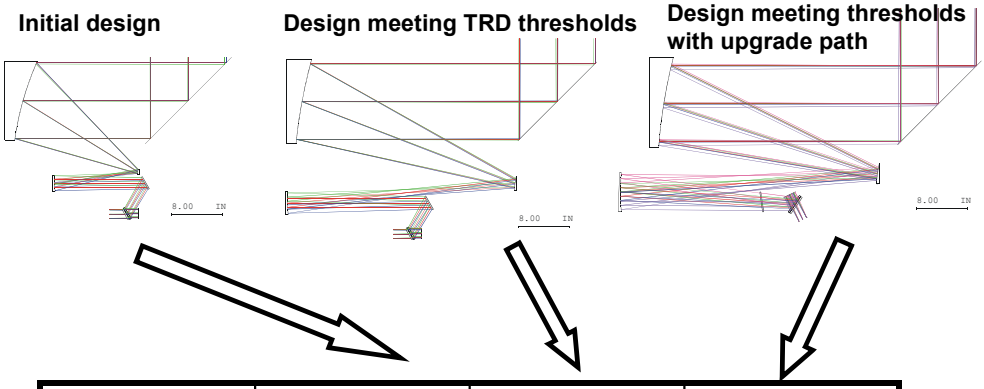

Field-of-View	160 x 480 km	220 x 530 km	500 x 530 km
Input Telescope Volume	0.9 x 0.6 x 0.3 meters	1.3 x 0.6 x 0.3 meters	1.3 x 0.7 x 0.3 meters

Figure 2-36. The growth in ABS point-design sensor volume with optical field.

Accounting for image rotation, it was necessary to expand the optical field of the point design by ~50% to 220 x 530 km. Figure 2-36 illustrates an approximately 50% increase in the volume of the input telescope (which drives the sensor volume) which can be attributed to this growth of field. Since most models for instrument volume and mass parameterize only against aperture diameter, this is a noteworthy result. The point design eventually arrived at in this work broadened the optical field to 530 x 250 km to provide for some upgradeability, with a negligible increase in sensor volume.

When earlier optical designs from References 2 and 3 are considered, as illustrated in Table 2-15, there is clearly a sensitive dependence on sensor volume with optical field. All six designs placed the optics in a common plane. In the 15-, 20-, and 25-cm designs, this was the N-S/E-W plane. In the 30-cm designs documented here, this is the E-W/nadir plane. In the dimension perpendicular to this plane, not surprisingly, there is only a slight variance with aperture and none with field. In the dimension in which the input telescope mirror axes are offset (N-S in the earlier designs, nadir in the present ones) there is a slight variance with both aperture and field, which is dictated by the need of optical elements to clear the ray bundles. In the dimension in which the input telescope mirrors are displaced axially (the E-W dimension in all designs) there is clearly a very large variation due to field alone due to clearance requirements and aberration effects, and it is this dimension that drives the growth in sensor volume commented upon in this report. Figure 2-37 illustrates the increase in instrument volume versus coverage rate for the completed instrument designs as the requirements have been modified to meet the requirements of the NWS, while showing that the 160 km x 480 km design fits into a one cubic meter volume.

Table 2-15. Dependence of ABS point-design volume on aperture and field.

Aperture diameter (cm)	GFOV (km)	Sensor dimensions including input telescope sunshade			
		N-S (m)	E-W (m)	Nadir (m) excluding radiators	Nadir (m) including radiators
15.24 (Ref. 2)	160 x 160	0.65	0.60	0.45	0.60
20.32 (Ref. 3)	120 x 120	0.70	0.70	0.55	0.60
25.4 (Ref. 3)	100 x 100	0.80	0.75	0.65	0.65
30.48 (this work)	160 x 480	0.70	1.00	1.15	1.15
	220 x 530	0.70	1.40	1.25	1.25
	250 x 530	0.70	1.65	1.20	1.20

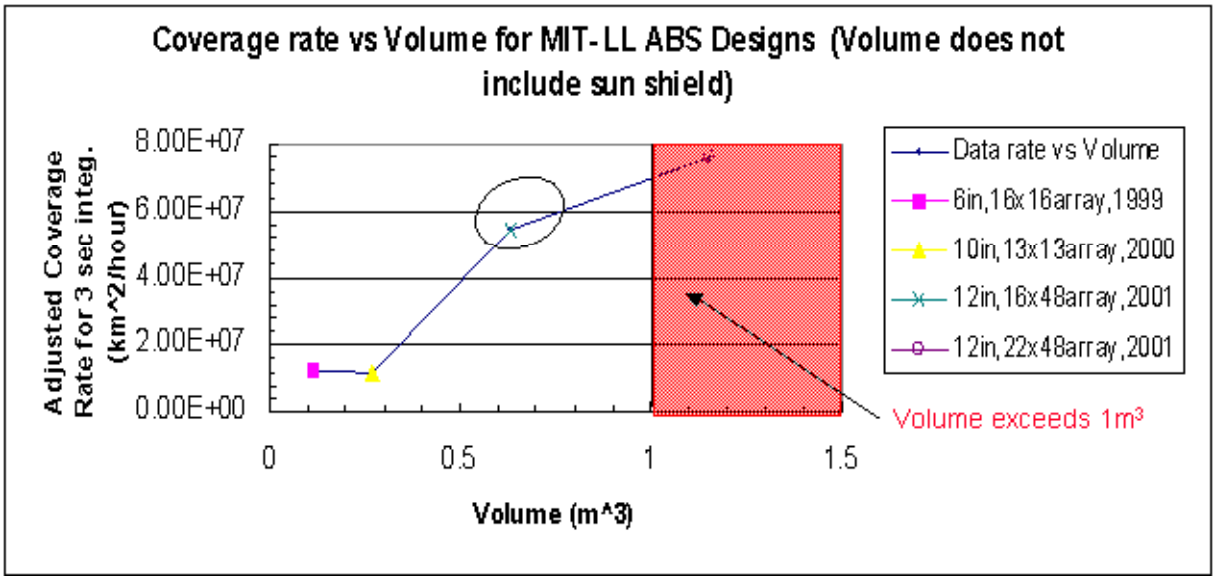

Figure 2-37. Instrument volume versus coverage rate increase, showing that the 160 km x 480 km fits in a one cubic meter volume.

The system mass estimate presented in Table 2-16, and the system power estimate presented in Table 2-17 are well in excess of the corresponding figures for the current sounder. The mass is largely dictated by the sensor volume, and by the multiple electronic signal processing chains that were needed to meet NEdN requirements. The power is substantially increased by the need for cryocooler refrigeration of the IR FPAs, which is necessary to meet coverage and NEdN needs. Again, the January 2001 TRD spacecraft accommodation "goals" are not met.

Table 2-16. ABS point-design system mass estimate.

Description	Mass (Kg)
Electronics mass estimate	
Power supplies (redundant set of 2 in shielded boxes)	10.0
Control electronics (redundant, See Table 2-10)	13.0
Signal processing electronics (redundant, see Table 2-12	8.0
Cryocooler electronics (redundant)	11.0
Cables	4.5
Power supplies and electronics mass estimate	46.5
20% contingency	9.3
ABS Sensor mass estimate (See Table 2-9)	~126
ABS System (sensor & electronics) mass estimate	**~185**

Table 2-17. ABS point-design system power estimate.

Description	Power (W)
ABS Electronics power estimate (See Table 2-13)	107
Power supply consumption (See Table 2-13)	36
Cryocooler compressor consumption (20 W/W at 2.5 W cold-tip load: See Table 2-7)	50
Cryocooler EOL margin	20
Cryocooler electronics power consumption	20
ABS System (sensor & electronics) power estimate	**~235**

Simply put, one of the conclusions of this study is that the NESDIS January 2001 TRD "thresholds" (to which this point design was formulated) and the NESDIS January 2001 TRD spacecraft accommodation "goals" are unlikely to be simultaneously met. We therefore defer further discussion of this issue to ongoing spacecraft accommodation studies, to which this point design forms an input. A comparison is made in Table 2-18 between the current (GOES-I) sounder and the ABS point design presented in this work.

Table 2-18. Spacecraft accommodation GOES-I / ABS point-design comparison.

Parameter	GOES-I [25]	ABS
Mass	126 Kg	185 Kg
Power	105 W	235 W
Volume (sensor)	137 x 80 x 75 cm	175 x 125 x 70 cm
Data rate	40 Kbps	< 10 Mbps

In order to address these spacecraft accommodation concerns and/or mitigate risk, we have examined a variety of cases that describe variations on the ABS point design, some of which do not meet the January 2001 TRD. The cases are described in Table 2-19 below. The NEdN values are listed in Table 2-20 and Table 2-21 and plotted in Figure 2-38. We await the latest version of the ABS January 2001 TRD requirements.

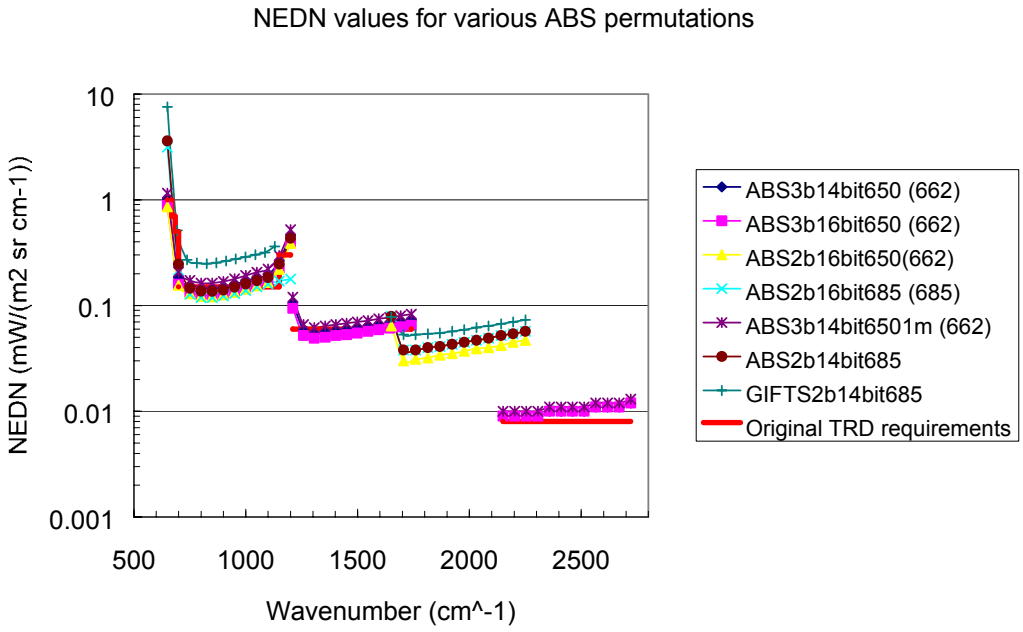

Figure 2-38. NEdN values for ABS excursion studies that either address associated spacecraft accommodation conscerns and/or mitigate risk, although some do not meet the January 2001 TRD.

Table 2-19. Spacecraft accommodation and risk reduction trade assumptions.

	Bands	LW ADC	Volume	Array size (GFOV)	Short name
ABS:3-band, 16-bit, ABS LW cutoff (MIT-LLPoint Design 2001) (median + family of curves	650-1200 cm^{-1} 1210-1740 cm^{-1} 2150-2720 cm^{-1}	16 bits	> 1 m^3	220 x 480 km^2	ABS3b16bit664
ABS:3-band, 14-bit, ABS LW cutoff (median + family of curves	650-1200 cm^{-1} 1210-1740 cm^{-1} 2150-2720 cm^{-1}	14 bits	> 1 m^3	220 x 480 km^2	ABS3b14bit664
ABS:2-band, 16-bit, ABS LW cutoff	650-1200 cm^{-1} 1650-2250 cm^{-1}	16 bits	> 1 m^3	220 x 480 km^2	ABS2b16bit664
ABS:2-band, 16-bit, GIFTS LW cutoff	685-1200 cm^{-1} 1650-2250 cm^{-1}	16 bits	> 1 m^3	220 x 480 km^2	ABS2b16bit685
ABS:2-band, 14-bit, GIFTS LW cutoff	685-1200 cm^{-1} 1650-2250 cm^{-1}	14 bits	> 1 m^3	220 x 480 km^2	ABS2b14bit685
ABS:3-band, 14-bit, ABS LW cutoff, 1 meter cube	650-1200 cm^{-1} 1210-1740 cm^{-1} 2150-2720 cm^{-1}	14 bits	< 1 m^3	160 x 480 km^2	ABS3b14bit6641m
ABS:2-band, 14-bit, GIFTS LW cutoff	685-1200 cm^{-1} 1650-2250 cm^{-1}	14 bits	> 1 m^3	512 x 512 km^2	GIFTS2b14bit685

Table 2-20. Spacecraft accommodation and risk reduction trade NEdNs.

	ABS3b14bit650(662)	ABS3b16bit650(662)	ABS3b14bit6501m(662)
Wavenumber (cm-1)	Total NEdN (14 bit)	Total NEdN (16 bit)	Total NEdN
650	1.025	0.886	1.155
700	0.184	0.159	0.208
750	0.153	0.133	0.173
800	0.145	0.126	0.163
850	0.145	0.125	0.163
900	0.15	0.129	0.169
950	0.159	0.137	0.179
1000	0.17	0.147	0.192
1050	0.183	0.158	0.207
1100	0.196	0.17	0.221
1150	0.263	0.226	0.296
1200	0.462	0.398	0.52
1210	0.106	0.094	0.12
1258	0.059	0.052	0.066
1306	0.054	0.049	0.062
1355	0.056	0.05	0.064
1403	0.058	0.052	0.066
1451	0.06	0.053	0.068
1499	0.062	0.055	0.07
1547	0.064	0.057	0.072
1595	0.066	0.059	0.075
1644	0.068	0.061	0.077
1692	0.071	0.063	0.08
1740	0.073	0.065	0.083
2150	0.009	0.009	0.01
2202	0.009	0.009	0.01
2254	0.009	0.009	0.01
2306	0.009	0.009	0.01
2358	0.01	0.01	0.011
2410	0.01	0.01	0.011
2461	0.01	0.01	0.011
2513	0.01	0.01	0.011

2565	0.011	0.011	0.012
2617	0.011	0.011	0.012
2669	0.011	0.011	0.012
2721	0.012	0.012	0.013

Table 2-21. More spacecraft accommodation and risk reduction trade NEdNs.

	ABS2b16bit 650(662)	ABS2b16bit 685 (685)	ABS3b14bit 6501m (662)	ABS2b14bit685	GIFTS2b14bit685
Wavenumber (cm-1)	Total NEdN	Total NEdN	Total NEdN	Total NEdN	NEDN(cal,8km)
650	0.861	3.139	1.155	3.6	7.559
700	0.155	0.215	0.208	0.246	0.512
750	0.129	0.128	0.173	0.146	0.27
800	0.122	0.119	0.163	0.137	0.252
850	0.121	0.119	0.163	0.136	0.249
900	0.126	0.123	0.169	0.14	0.254
950	0.133	0.13	0.179	0.149	0.264
1000	0.143	0.139	0.192	0.16	0.275
1050	0.154	0.15	0.207	0.172	0.288
1100	0.165	0.16	0.221	0.184	0.302
1150	0.22	0.17	0.296	0.246	0.317
1200	0.387	0.178	0.52	0.433	0.362
1650	0.064	0.079	0.12	0.079	0.078
1705	0.03	0.038	0.066	0.038	0.053
1759	0.031	0.038	0.062	0.038	0.053
1814	0.032	0.04	0.064	0.04	0.054
1868	0.034	0.041	0.066	0.041	0.055
1923	0.035	0.043	0.068	0.043	0.057
1977	0.037	0.045	0.07	0.045	0.059
2032	0.039	0.047	0.072	0.047	0.062
2086	0.04	0.049	0.075	0.049	0.064
2141	0.042	0.052	0.077	0.052	0.067
2195	0.045	0.054	0.08	0.054	0.07
2250	0.047	0.057	0.083	0.057	0.073

2.10 Comments On Science Benefit and Technology Readiness

2.10.1 Addressing January, 2001 TRD "Top Priorities" and "Goals"

The NWS ORD[5] and the NESDIS January 2001 TRD [1] both voiced a strong need for future GOES sensors to address technical issues which have proved detrimental to past operations. With respect to atmospheric sounding, the identified "top priority" issues are:

1. Continuous operation of the sensor through periods when the satellite is in eclipse, and

2. Minimizing so-called "keep out zones" which restrict data collection near the Earth limb in the vicinity of the Sun as it transits behind the Earth during eclipse.

Both of these issues cause substantial loss of data, and reduction of the quality of data, in the current GOES sounder. Measures taken in the ABS point design to address these issues are highlighted below.

Operation through eclipse. Beginning with the launch of GOES-N in 2004, the GOES spacecraft will provide sufficient battery capacity to keep the sensors operating through satellite eclipse. The primary concern in the point design is therefore the quality of data obtained during eclipse. One problematic issue has been distortion of the beryllium scan mirror under conditions of solar heating. The ~5 times greater stiffness to CTE ratio of the SiC scan mirror assumed in this point design should greatly mitigate this problem. A second problem is that the abrupt removal of sunlight causes thermal transients to occur in the radiative coolers, and transient distortions of structures to occur due to CTE effects. These can cause radiometric and line-of-sight errors. The use of cryocoolers means that there will be far less sensitivity to eclipse transients in the ABS point design, while the use of OSR's for the radiators means that these ought to be less sensitive to transients as well. This should minimize radiometric errors. Thermal distortion of the structure remains a problem, although one which can be addressed in the formulation phase through judicious design.

Minimizing "keep out zones". As was the case with the point design of Reference 2, the single largest measure taken to mitigate this effect is the use of an off-axis telescope design. This eliminates the focusing of out-of-field sunlight onto the secondary mirror support that occurs in the current GOES sounder design. In addition, the availability of accessible images for the insertion of field stops means that the ABS point design documented here can have significantly reduced stray radiation from out-of-field sources.

Performance enhancement through modularity. Several measures were taken in this point design to enhance performance beyond the "threshold" requirements of the January 2001 TRD. One case is the incorporation of a dedicated low-light imaging channel which provides cloud detection in twilight and some moonlit conditions. Since the original design of Reference 2 incorporated a neutral-density filter to avoid saturating the CCD during interferogram acquisition, it was straightforward to replace this with a

beamsplitter that directed most of the light to a CCD, which is permitted to saturate under full-albedo illumination.

A second instance was the decision to design the optical system for a wider field than would be populated by the CCD's and IR FPA's. This was undertaken in order to provide margin during the design process, and because it permitted modular replacement of the detector arrays with larger-format units should technology (and data-rate limitations) permit. This holds the possibility of modest improvements in coverage and/or sensitivity. Most of the volume penalty incurred in moving to a wider-field input telescope was incurred in going from an interim 480 x 160 km design to a 530 x 220 km version which was necessary to meet the January 2001 TRD coverage rate and NEdN thresholds simultaneously. The final optical design provides a 530 x 500 km visible field (populated by 480 x 220 km CCD's) and a 530 x 250 km IR field (populated by 480 x 220 km IR FPA's). This was obtained with a negligible increase in volume.

Because ample margin has been budgeted into the cryocooler design, concerns associated with increased focal plane power dissipation are less of a concern than limitations in the GOES data downlink, which placed a 10 Mbit/s upper limit on the ABS data rate. Should future developments in the GOES communications system provide greater capacity, sensor upgradeability is an attractive feature.

2.10.2 Infusion of GIFTS Technology

Since the original ABS design study documented in Reference 2, the NASA Langley Research Center (LaRC) has been developing a geostationary water vapor imager and atmospheric sounder under the New Millennium Program. The GIFTS sensor develops numerous technologies that are relevant to ABS and the ongoing progress on GIFTS has been a major impetus in the evolution of science requirements embodied in the NESDIS January 2001 TRD.

Several GIFTS technologies are leveraged partially or fully for this ABS point design, in particular:

1. The high-efficiency pulse-tube cryocooler utilized in this point design has essentially the same compressor and electronics as the GIFTS cryocooler. The only difference is our use of the previously developed cold head rather than the GIFTS sensor's two-stage cold head which was required because GIFTS uses the cryocooler to refrigerate the aft optics to ~150 K.

2. The porch-swing mechanism and commandable mirror mechanism, although based on MIT/LL work on the polar Interferometer Thermal Sounder (ITS) are similar to the GIFTS units.

3. The scan mirror uses the same silicon carbide construction as GIFTS. Substantial similarity in the motor and mechanisms is assumed as well.

2.11 Technology Risk Areas and Long-Life Issues

In this section, we briefly comment on some aspects of the ABS point design that warrant attention with respect to risk and/or lifetime. The requirements of Section 1 call for an instrument design life of 10 years to support a 7-year GOES mission duration. The system components listed below are, in our estimation, those which merit further (and in some cases ongoing) examination is justified to meet this lifetime with acceptable risk. It is noteworthy that in the case of the metrology laser and the 16-bit A/D converters, part of the risk is that a lack of vendor support for space programs may be encountered since these are essentially COTS (commercial off-the-shelf) items.

Interferometer metrology source

Risk: Low/Moderate

This point design assumes a ~1500 nm laser to provide sampling knowledge during the FTS moving mirror stroke. The GOES High-Resolution Interferometric Sounder (GHIS) brassboard used a commercial 1532 nm laser modified for a space application. This point design assumes a similar course of action. Implementation of a redundant metrology source is highly desirable, though it was not addressed in this work.

Fast 16-bit space-qualified A/D converter

Risk: Low/Moderate

This point design assumes 16-bit A/D converters in the MWIR and LWIR channels. Although commercially available parts can provide the needed performance, there are not presently any space-qualified versions. This point design assumes that repackaging and shielding of commercial A/D converters can be implemented, but this entails risk.

Cryocooler lifetime

Risk: Low/Moderate

The continuous operation of cryocoolers over ~10-year durations has not been demonstrated, either in the laboratory or on-orbit. Technology validation will be provided by GIFTS, but that sensor does not have the lifetime requirements of ABS.

LWIR Detector technology readiness

Risk: Low/Moderate

Ongoing work at MIT/LL has served to mitigate this risk, but the ~15 μm cutoff wavelength required for the longwave ABS band is near the limit of current technology for PV detectors at 65 K. Large (~ 1000 pixel) longwave PV detector technology is immature and lacks a spaceflight heritage. A custom high-performance readout IC is required as well. Risk reduction will be provided by GIFTS unless a de-scope causes the LWIR band to be dropped from that sensor.

Wide-field, fast, off-axis optical system

Risk: Low

The ABS point design places substantial demands on the optical design, particularly with respect to tolerancing, alignment, and closely-spaced spectral bands. GIFTS provides risk reduction, since it has similar requirements for system optics.

Lack of margin

Risk: Low/Moderate

Although this point design meets the January 2001 TRD thresholds, in several important respects such as NEdN, coverage and data rate, it does so with zero margin. Although not a technological risk, insufficient margin is clearly a long-life issue. It is expected that continued evolution of requirements will mitigate this risk.

APPENDIX A. LIST OF ACRONYMS

ABS	GOES Advanced Baseline Sounder
A/D or ADC	Analog-to-digital converter
ASIC	Application-specific integrated circuit
BDI	Buffered direct-injection
BLIP	Background-limited infrared photodetection
CCD	Charge-coupled device
CONUS	Continental United States
COTS	Commercial, off-the-shelf
CTE	Coefficient of thermal expansion
CTIA	Capacitive transimpedance amplifier
DSP	Digital signal processor
E-W/N-S	Satellite coordinate system (east-west, north-south, nadir)
EOL	End of life
FIR	Finite impulse-response
FOR	Field of regard
FOV	Field of view
FPA	Focal-plane array
FTS	Fourier-transform spectrometer
G-10	Fiberglas-epoxy laminate
GHIS	GOES High-resolution Interferometric Spectrometer
GIFTS	Geostationary Imaging Fourier Transform Spectrometer
GOES	Geostationary Operational Environmental Satellite
HgCdTe	Mercury Cadmium Telluride
IR	Infrared
ITS	Interferometer Thermal Sounder
LWIR	Long-wavelength infrared

MIT/LL	Lincoln Laboratory, Massachusetts Institute of Technology
MWIR	Mid-wavelength infrared
NASA	National Aeronautics and Space Administration
NEdN	Noise-equivalent differential (or delta) radiance
NEdT	Noise-equivalent differential (or delta) temperature
NESDIS	National Environmental Satellite, Data, and Information Service
NMP	New Millennium Program
NOAA	National Oceanic and Atmospheric Administration
NWS	National Weather Service
OPD	Optical path difference
ORD	Operational Requirements Document
OSR	Optical surface reflector
PORD	Performance and Operational Requirements Document
PV	Photovoltaic
ROIC	Readout integrated circuit
SiC	Silicon carbide
SiO_x	Silicon oxide / silicon dioxide mixture
SNR	Signal-to-noise ratio
SS	Stainless steel
SSP	Satellite sub-point
SWIR	Short-wavelength infrared
TBD	To be determined
TRD	Technical Requirements Document
Y_2O_3	Yttrium oxide
ZnSe	Zinc selenide

REFERENCES

1 "NOAA's Technical Requirements for a Geostationary Advanced Baseline Sounder (ABS)," National Environmental Satellite, Data, and Information Service (NESDIS), January, 2001.

2 L. Candell, M. MacDonald, G. Carlisle, M. Coakley, H. Finkle, M. Kelly, D. Ryan-Howard, D. Weidler, D. Weitz, "Advanced Baseline Sounder Design Study," Project Report NOAA-24, MIT Lincoln Laboratory, 28 January, 1999.

3 M. E. MacDonald, M. Kelly, D. P. Ryan-Howard, E. C. Wack, "GOES Advanced Baseline Sounder (ABS) Design Changes for Improved Spatial Performance," Project Report NOAA-28, MIT Lincoln Laboratory, 6 April, 2000.

References 2 and 3 have been summarized for the open literature in "Architectural trades for an advanced geostationary atmospheric sounding instrument," M. E. MacDonald, E. C. Wack, M. W. Kelly, D. P. Ryan-Howard, M. M. Coakley, H. R. Finkle, D. E. Weidler, D. M. Weitz, G. W. Carlisle, L. M. Candell, Proceedings of the 2001 IEEE Aerospace Conf., Big Sky, MT, March, 2001.

4 Draft document, "Observational Requirements for the Evolution of Future NOAA Operational Geostationary Satellites," National Weather Service, 12 December, 1996.

5 National Weather Service, "Operational Requirements for Future Geostationary Operational Satellites," J. J. Kelly, 8 January, 1999.

6 G. W. Carlisle, "Novel Scan Technique to Remove Band-to-Band Co-registration Error" attachment in *Appendix C, ABI Material*, MIT/LL ABI Papers and Briefing (other than Quarterlies), Addendum to ABI Phase A Report, performed under U.S. Air Force Contract F-19628-95-C0002.

7 Henry E. Revercomb, H. Buijs, Hugh B. Howell, D. D. LaPorte, William L. Smith and L. A. Sromovsky, "Radiometric calibration of IR Fourier transform spectrometers: solution to a problem with the High-Resolution Interferometer Sounder," *Appl. Opt.*, Vol. 27, No. 15, pp 3210-3218 (1988).

8 M. M. Coakley, G. D. Berthiaume, J. A. Shultz, "Large IR Focal Plane Array Characterization for GOES", SPIE International Symposium on Optical Science and Technology, 30 July – August 4, 2000, Earth Observing Systems V, SPIE meeting proceedings vol. 4135.

9 M. E. MacDonald, "Investigation of alternates to SiO_x for protective scan mirror coatings in remote sensing instruments," *SPIE Proc.* Vol. 3750, pp. 309-318 (1999).

10 M. Weinreb, M. Jamieson, N. Fulton, Y. Chen, J. Xie Johnson, J. Bremer, C. Smith, and J. Baucom, "Operational calibration of geostationary operational environmental satellite -8 and -9 imagers and sounders," *Appl. Opt.*, Vol. 36, No. 27, pp 6895-6904 (1997).

11 J. L. Vampola, "Readout electronics for infrared sensors" in *The Infrared and Electro-Optical System Handbook*, Vol. 3, "Electro-optical Components," W. D. Rogatto (Ed.), SPIE Press, 1993.

12 D. L. Mooney, D. R. Bold, M. S. Cafferty, D. L. Cohn, H. J. Jimenez, J. P. Kerkes, R. W. Miller, M. J. Persky, D. P. Ryan-Howard, "POES Advanced Sounder Study (Phase II), Lincoln Laboratory Internal Project Report NOAA-7, March 17, 1994.

13 M. W. Kelly, M. J. Gazarik, and R. M. Marino, "Noise performance of the NPOESS airborne sounder testbed interferometer (NAST-I) sounder: flight and model results," *Proc. SPIE* Vol. 3750, pp. 260-268 (1999).

14 R. G. Ross, "Cryocooler reliability considerations for long-life space missions," *Cryocoolers 11* (2000).

15 See, for example, D. S. Glaister, et. al., *Cryocoolers 10*, pp. 1-19 (1998), G. S. Mand, et. al., *Cryocoolers 11* (2000), R. G. Ross, et. al., *Cryocoolers 10*, pp 119-128 (1998), B. J. Tomlinson, et. al., *Cryocoolers 10*, pp. 129-138 (1998), C. K. Chan, et. al., *Cryogenics* Vol. 39, pp. 1007-1014 (1999).

16 E. Tward, T. Davis, *AIAA Proceedings* (2000).

17 NASA Langley Research Center, "Geostationary Imaging Fourier Transform Spectrometer (GIFTS) Concept Study Report," September, 1999.

18 M. M. Coakley, G. D. Berthiaume, J. A. Shultz, "Large IR Focal Plane Array Characterization for GOES", SPIE International Symposium on Optical Science and Technology, 30 July – August 4, 2000, Earth Observing Systems V, SPIE meeting proceedings vol. 4135.

19 Graham Walker, "Cryocoolers", Plenum, New York, 1983.

20 W. E. Bicknell, et. al., "GOES High-Resolution Interferometer Sounder (GHIS) Brassboard Test Program," Project Report NOAA-22, MIT Lincoln Laboratory, July, 1998.

21 W. E. Bicknell, et. al., "GOES High Resolution Interferometer Study," Project Report NOAA-12, MIT Lincoln Laboratory, June, 1995.

22 D. L. Mooney, et. al., "POES High-resolution sounder study final report," Project Report NOAA-1, MIT Lincoln Laboratory, 1993.

23 “CrIS Weather Product Test Bed: AIRS simulated orbit and NOAA radiosonde data set”, Sept. 21, 1998.

24 "NOAA's Technical Requirements for a Geostationary Advanced Baseline Sounder (ABS)," National Environmental Satellite, Data, and Information Service (NESDIS), January, 2001.

25 Stanley Q. Kidder, Thomas H. Vonder Haar, "Satellite Meteorology," Academic Press, San Diego, 1995.